4 PRESENTATION AND DISCUSSION OF EXPERIMENTAL AND COMPUTATIONAL RESULTS

4.1 Experimental results overview

Schlieren images for the eight rectangular, eight triangular, three parabolic and two conical valley test pieces are obtained at several sequential time delays to determine the development of the resulting wave structures. Shadowgraph images of the rectangular valleys (60 degree wedge) at zero and fifteen degree valley floor inclination, as well as the rectangular valley (70 degree wedge) at forty-five degree valley floor inclination, are presented to validate the reflection off the valley floor. Schlieren images at several sequential time delays are also presented for the three hill geometries (triangular, parabolic and conical). All experimentation was carried out with an incident shock wave strength of Mach 1.4.

4.2 Computational results overview

Three dimensional computational results were accomplished with the use of a CFD software programme. A three-dimensional inviscid, unsteady, coupled, explicit solver was used to model the fluid flow. Two-dimensional images of the resulting shock wave structures were generated by taking slices of the three-dimensional flow field in the y-z plane. These images were then analysed and compared to the schlieren images obtained experimentally. Two-dimensional images were also generated in the x-y plane to analysis the transverse flow characteristics. Three-dimensional images were generated to analysis and validate the existence of the complex three-dimensional wave structures. After close inspection of both the two- and three-dimensional images, three-dimensional NURBS (non-uniform rational B-splines) models of the wave structures for four rectangular and four triangular valleys were produced to illustrate the findings more effectively.

All experimental and computational results used for the analysis of the resulting complex wave structures are presented for the rectangular valley $\theta_w = 60^\circ$, $\theta_v = 0^\circ$. In order to slim down the amount of pictures presented in the body of this project report only the first test piece for each of the valley/hill geometries is discussed in similar detail. The results for the rest of the test pieces are then summarised with respect to this detailed analysis. The images similar to those presented in the first detailed description can be found in appendix E for all test pieces. Any other images used in the analysis not shown in the body of the report or in Appendix E can be found on a CD included in Appendix F.

4.3 Rectangular valley results

4.3.1 Rectangular valley, $\theta_w = 60°$, $\theta_v = 0°$

Schlieren and shadowgraph images are presented in figure 4.1 and figure 4.2. The images are taken at sequential time delays. With the incorporation of the glass piece on all rectangular valleys, the shock wave reflections off both the wedge and valley floor surfaces can be depicted. The incident shock wave initially only reflects off the wedge surface as regular reflection. As it advances further downstream two reflections start to appear, regular reflection off the wedge surface and Mach reflection off the valley floor for a zero degree inclination. A sonic wave generated at the valley entrance is seen in all schlieren images, as well as the effect of the sonic wave from the first corner (bottom of wedge). The further downstream the incident shock moves, the greater the influence of the sonic wave becomes on the reflected shock. The suggested three-dimensional wave structure is also depicted from the schlieren images, due to the different positions of the two reflected waves. Although a slip stream is expected from the Mach reflection off the valley floor, it can not be seen in the images due to the sensitivity of the optical system.

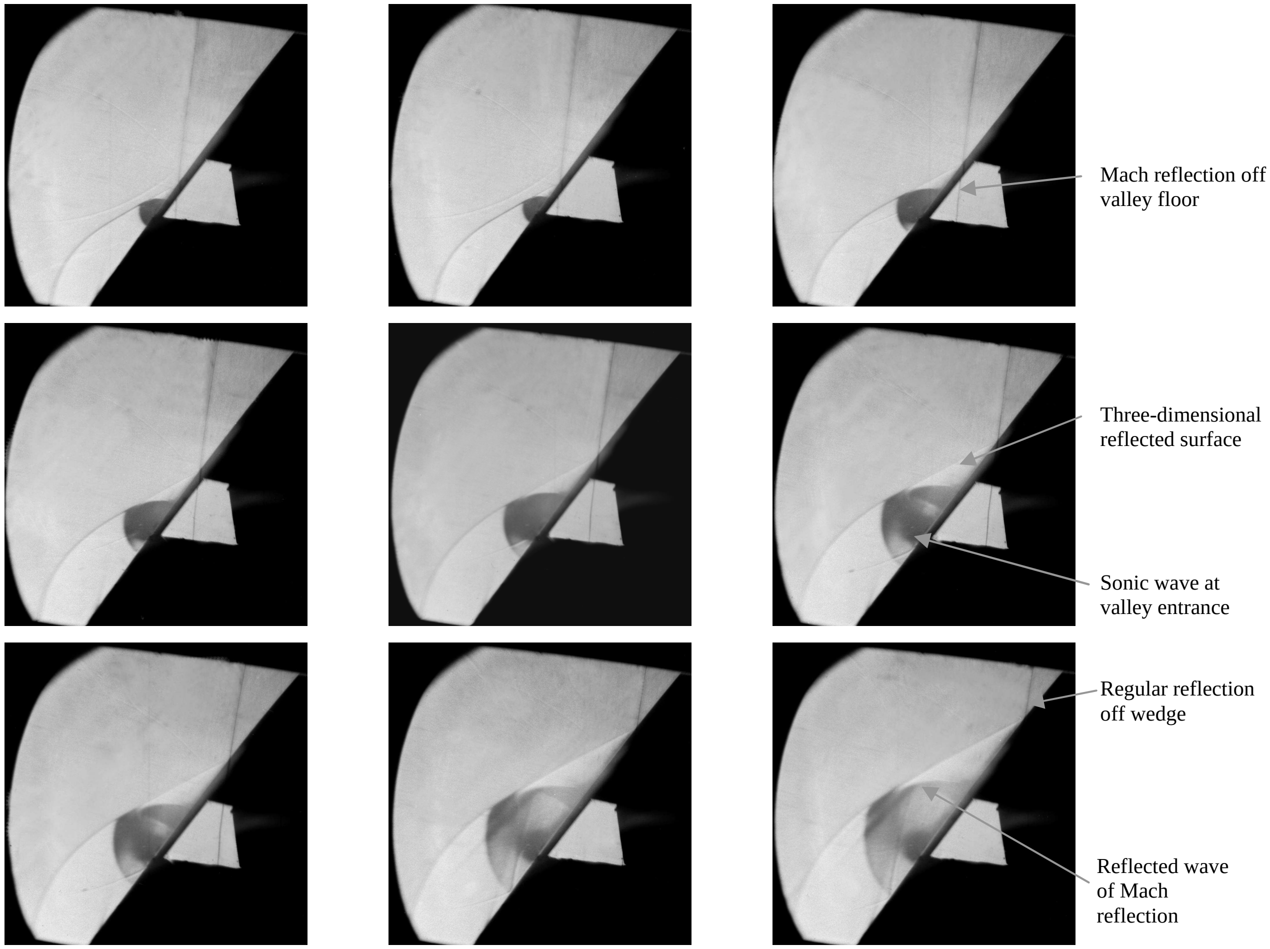

Figure 4.1: Schlieren images for rectangular valley, $\theta_w = 60^o$, $\theta_v = 0^o$, at time delay 1655μs, 1665μs, 1675μs, 1685μs, 1695μs, 1705μs, 1715μs, 1725μs and 1735μs respectively.

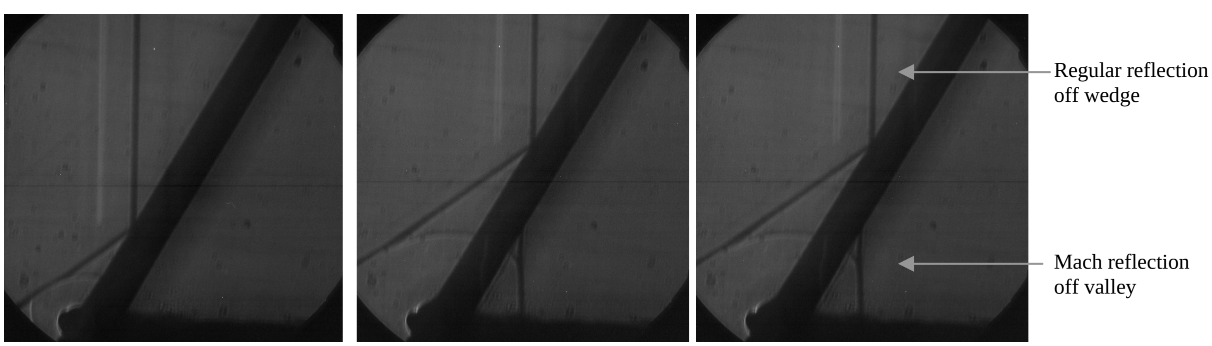

Figure 4.2: Shadowgraph images for rectangular valley, $\theta_w = 60^o$, $\theta_v = 0^o$, at time delay 1660μs, 1670μs and 1680μs respectively.

Numerical two-dimensional images were produced from the three-dimensional solution by superimposing planes taken at 18.75mm and 56.25mm along the x-axis (planes at exactly half the wedge width and at exactly half the valley width). Similar images were produced for all valley and hill geometries to aid in the validation of the experimental results. The two-dimensional images were taken at sequential time steps which allowed the reflection off the wedge and valley floor surfaces to be analysed and compared directly to the schlieren and shadowgraph images obtained experimentally. The regular reflection off the wedge surface and the Mach reflection off the valley floor are depicted in the images presented in figure 4.3, and compare directly with the experimental results. A shear layer is also depicted in these images at the valley entrance. As the incident shock advances downstream the shear layer tends to increase with size. The sonic wave generated by both the wedge and valley entrance corners is also depicted in these images. One can also see the increased influence of the sonic waves on the reflection as the incident shock advances downstream. A weak slip stream is also present in these images.

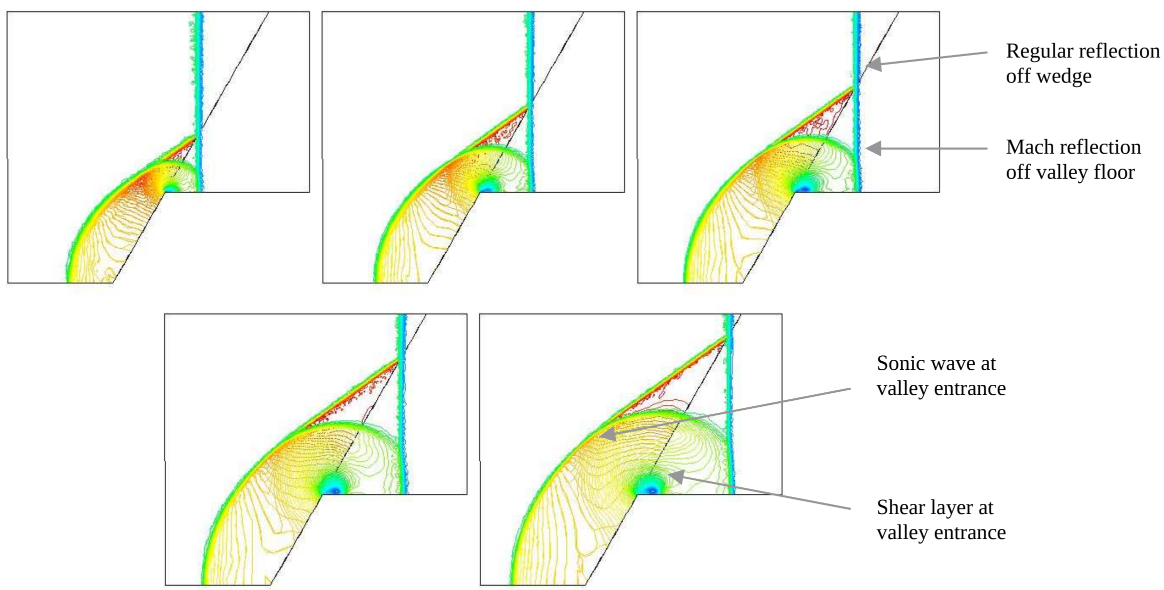

Figure 4.3: Time sequential density contour plots for rectangular valley, θ_w = 60º, θ_v = 0º.

In order to determine how the regular reflection off the wedge surface and the Mach reflection off the valley floor merge and form a three-dimensional reflected shock surface, planes along the x axis were taken at a single time step. The planes also depict how the wave structures change across the width of the test piece. The images are presemted in figure 4.4. The regular reflection off the wedge surface is seen in the first three images. Mach reflection is seen to occur off the valley floor in the rest of the images. The Mach reflection occurs underneath the reflected wave off the wedge surface. The reflected wave off the wedge surface, which flows over into the valley, is referred to as the primary reflected wave for all rectangular valleys. The resulting reflected wave of the Mach reflection off the valley floor is referred to as the secondary reflected wave for all rectangular valleys. The primary reflected wave flows over into the valley and contacts the incident wave at a second contact point found above the triple point. The section of the incident wave between the second contact point and the triple point is seen to slightly bow into the downstream flow. The distance between the second contact point and the triple point decreases as one moves closer to the symmetry plane (x = 75mm), and at a point near the symmetry plane they coincide. The secondary reflected wave merges with the primary reflected wave near the symmetry plane and again at the wedge surface. The shear layer at the valley entrance found in figure 4.3, is depicted in these images and travels along the full length of the valley entrance. The presence of a second shear layer is also found cascading down the valley wall. The two sonic waves developed at the wedge and valley entrance corners are also depicted in the images. A weak slip stream is also seen in last images.

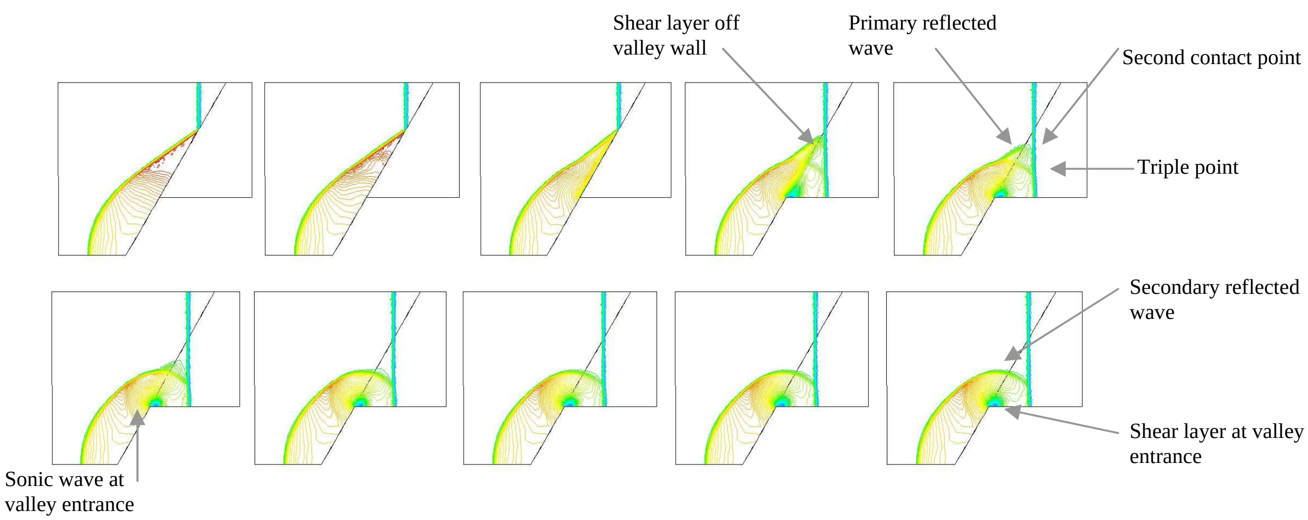

Figure 4.4: Density contour plots for rectangular valley, $\theta_w = 60^o$, $\theta_v = 0^o$, taken in the y-z plane at x = 0mm, 18.75mm, 37.5mm, 42.5mm, 47.5mm, 52.5mm, 57.5mm, 62.5mm, 68.75mm, 75mm respectively.

A few planes taken along the x axis shown in figure 4.4 are enlarged in figure 4.5 in order to fully understand the reflection phenomenon. The Mach reflection off the valley floor, the shear layer cascading down the valley wall, the shear layer along the valley entrance, the primary and secondary reflected waves, the second contact point and the triple point are all be depicted in these images. The slight bowing of the incident wave between the second contact point and the triple point is depicted in these images. The weak slip stream is depicted more clearly in these images.

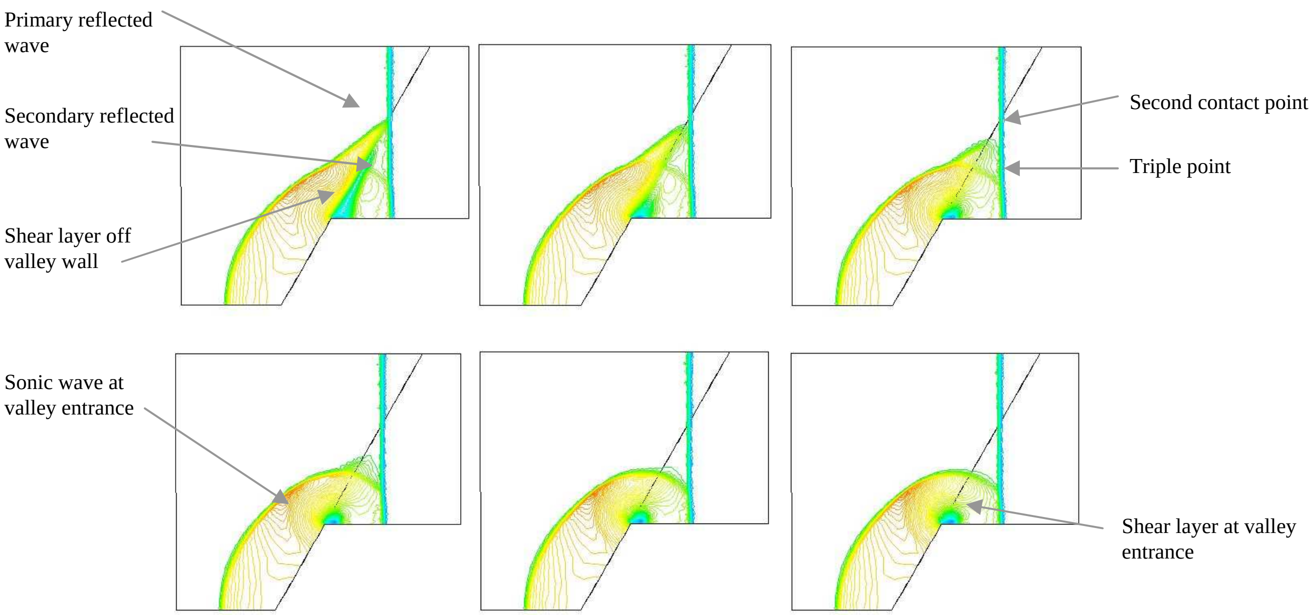

Figure 4.5: Enlarged density contour plots for rectangular valley, $\theta_w = 60^o$, $\theta_v = 0^o$, taken in the y-z plane at x = 40mm, 42.5mm, 47.5mm, 52.5mm, 57.5mm, 62.5mm respectively.

In order to fully decipher the reflection off the valley floor and the resulting secondary reflected wave single level pressure contour plots were generated at planes along the x axis (figure 4.6). The Mach reflection off the valley floor is found to continue across the entire width of the valley. The secondary reflected wave becomes slightly distorted near the valley wall as the surface climbs up the wall changing to regular reflection at the wedge surface. By superimposing all the planes in figure 4.6 the three-dimensional reflection surface of the secondary reflected wave is illustrated in figure 4.7. The shear layer cascading down the valley wall can be seen to merge with the shear layer generated at the valley entrance. By increasing the number of levels of the contours in figure 4.7, but keeping the pressure constant, figure 4.8 is generated. This figure illustrates the secondary reflected surface in a more solid from.

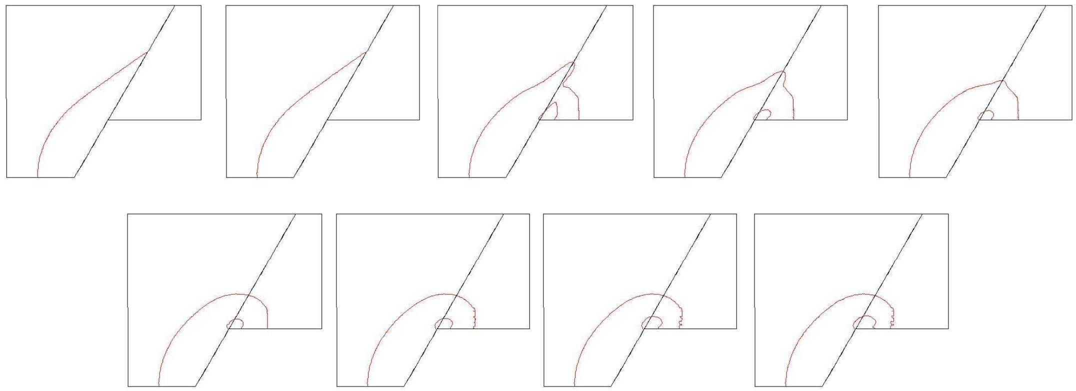

Figure 4.6: Pressure contour plots (single level) of secondary reflected wave for rectangular valley, $\theta_w = 60°$, $\theta_v = 0°$, taken in the y-z plane at x = 0mm, 18.75mm, 37.5mm, 42.5mm, 47.5mm, 52.5mm, 57.5mm, 62.5mm, 68.75mm, 75mm respectively.

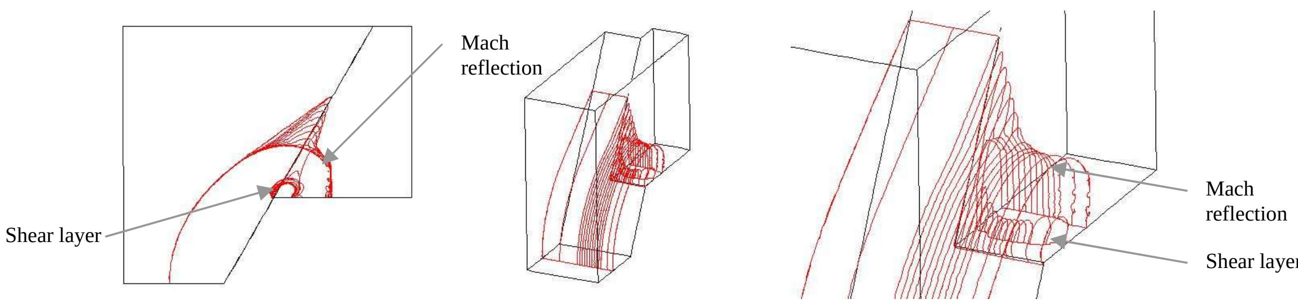

Figure 4.7: Superimposed pressure contour plots (single level) of secondary reflected wave for rectangular valley, $\theta_w = 60°$, $\theta_v = 0°$.

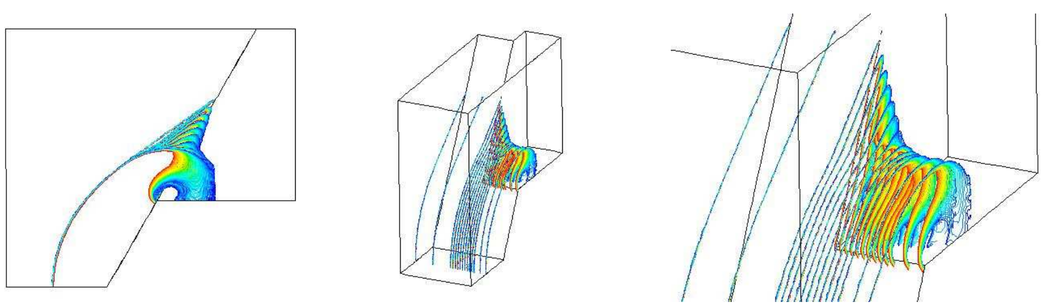

Figure 4.8: Superimposed pressure contour plots (multiple levels) of secondary reflected wave for rectangular valley, $\theta_w = 60°$, $\theta_v = 0°$.

In order to develop a complete three-dimensional understanding of the resulting wave structures, planes along the z axis were generated. Isometric and front views of these planes are shown in figures 4.9 and 4.11 respectively. The isometric views illustrate once again the presence of the two shear layers. They also illustrate the presence of a Mach reflection in the x-y plane. A double triple point and two Mach stems are seen in the images. The analysis of this phenomenon is beyond the scope of this research however, its presence is noted. The front views of these planes also depicted the sloping of the primary reflected wave as it flows over into the valley. The further the flow penetrates downstream, the steeper the surface becomes. The last image in the figure 4.11 depicts the path of the second contact point (***A***) as it travels along the incident wave between the valley wall and the symmetry plane. The second contact point follows a negatively sloping path from the wedge surface until it is coincident with the triple point close to the symmetry plane. The presence of an expansion wave can also be seen along the surface of the wedge. Figure 4.12 merely enlarges the images generated in figure 4.11 for better clarity of the problem.

By overlaying all the planes generated along the z axis, Figure 4.10 illustrates the primary reflected wave in an isometric view and figure 4.13 illustrates the primary reflected wave in a front view. When these figures are compared, the surface is seen to almost form a conical shape around the wall of the valley.

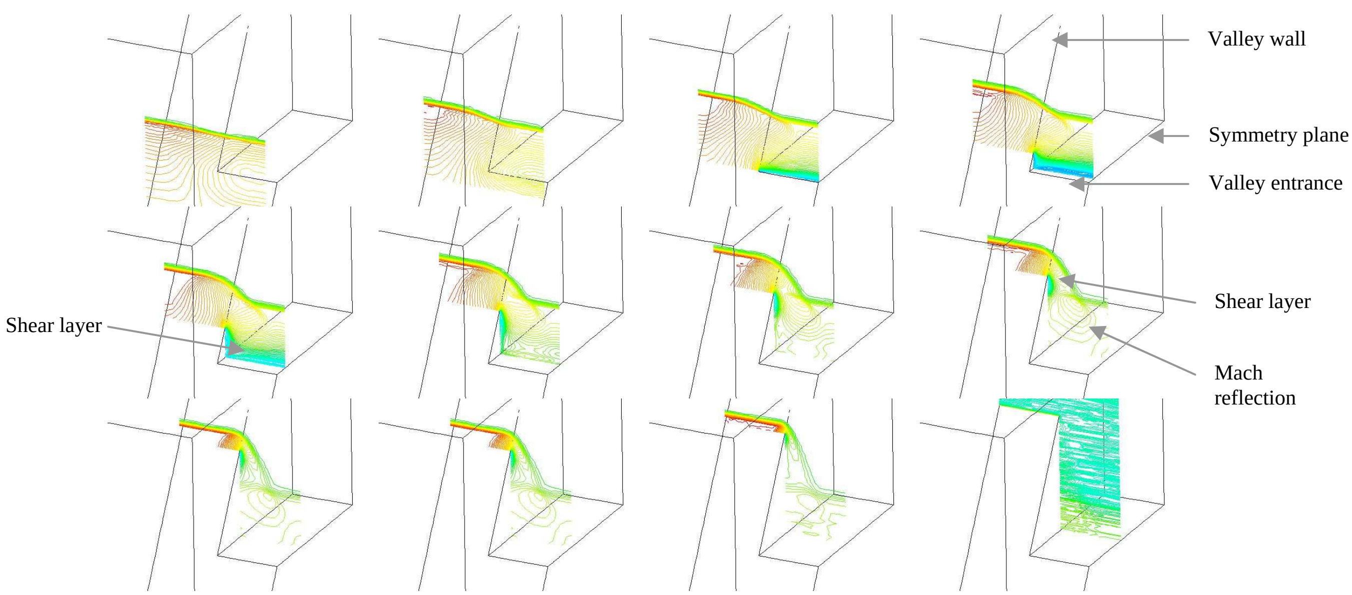

Figure 4.9: Isometric views of sequential density contour plots for rectangular valley, θ_w = 60º, θ_v = 0º, taken in the x-y plane in steps of 5mm along the z axis.

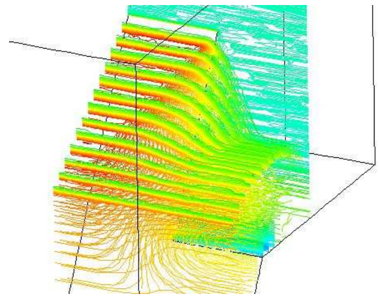

Figure 4.10: Isometric view of superimposed density contour plots for rectangular valley, $\theta_w = 60^o$, $\theta_v = 0^o$, taken in the x-y plane.

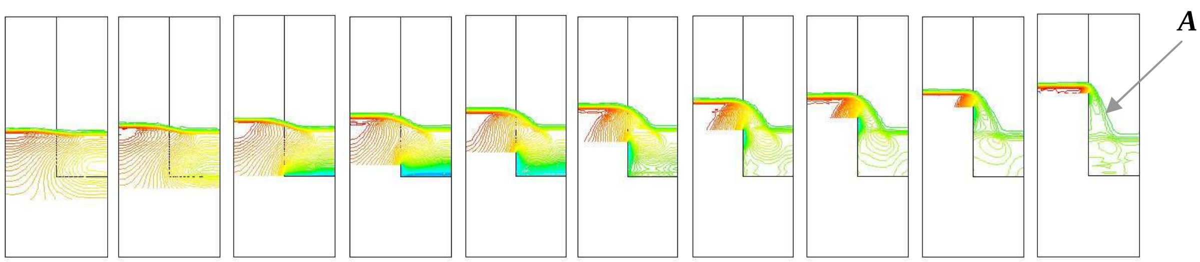

Figure 4.11: Sequential density contour plots for rectangular valley, $\theta_w = 60^o$, $\theta_v = 0^o$, taken in the x-y plane in steps of 5mm along the z axis.

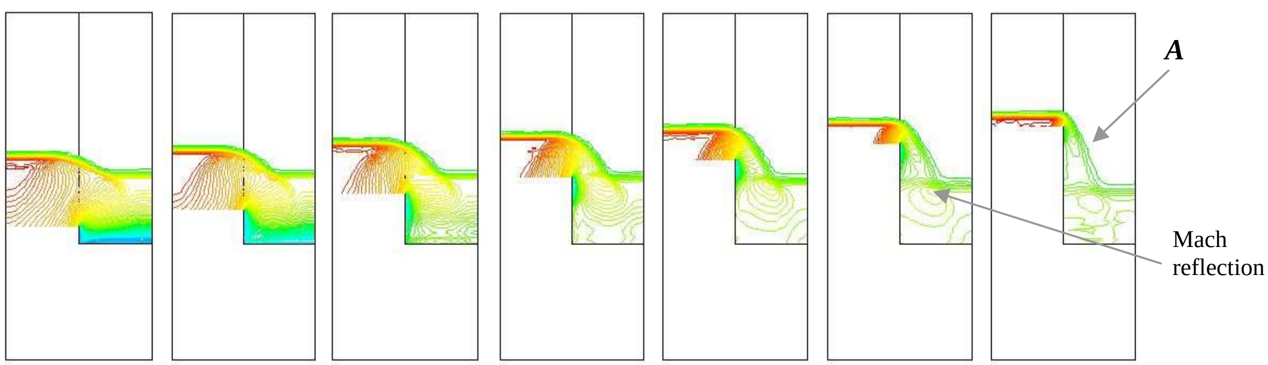

Figure 4.12: Enlarged sequential density contour plots for rectangular valley, $\theta_w = 60^o$, $\theta_v = 0^o$, taken in the x-y in steps of 5mm along the z axis.

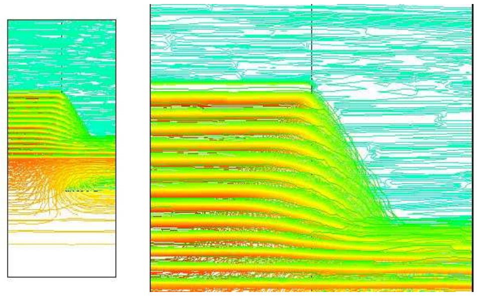

Figure 4.13: Superimposed density contour plots for rectangular valley, $\theta_w = 60^o$, $\theta_v = 0^o$, taken in the x-y plane.

By taking filled density contour plots of planes along the x axis the presence of the shear layer along the valley entrance is depicted. This is shown in figure 4.14.

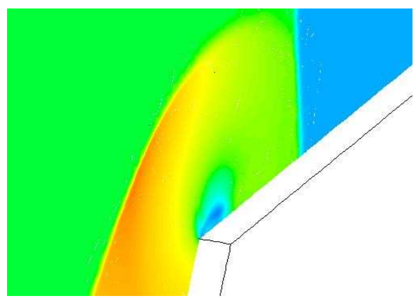

Figure 4.14: Filled density contour plot of a y-z plane for rectangular valley, $\theta_w = 60^o$, $\theta_v = 0^o$, illustrating shear layer.

To obtain a complete three-dimensional image of the reflected shock surface planes along the x and z axes are superimposed, as shown in figure 4.15a. The incident shock, the primary reflected wave, the regular reflection off the wedge, the Mach reflection off the valley floor, the shear layer at the valley entrance, the sonic wave generated at the valley entrance and the expansion wave on the wedge surface can all be seen in the figure. However, the secondary reflected wave is covered by the primary reflected wave surface. To illustrate the three-dimensional surface of the secondary reflected wave, figure 4.15b is presented. The shear layers at the valley wall and entrance are also seen in this image.

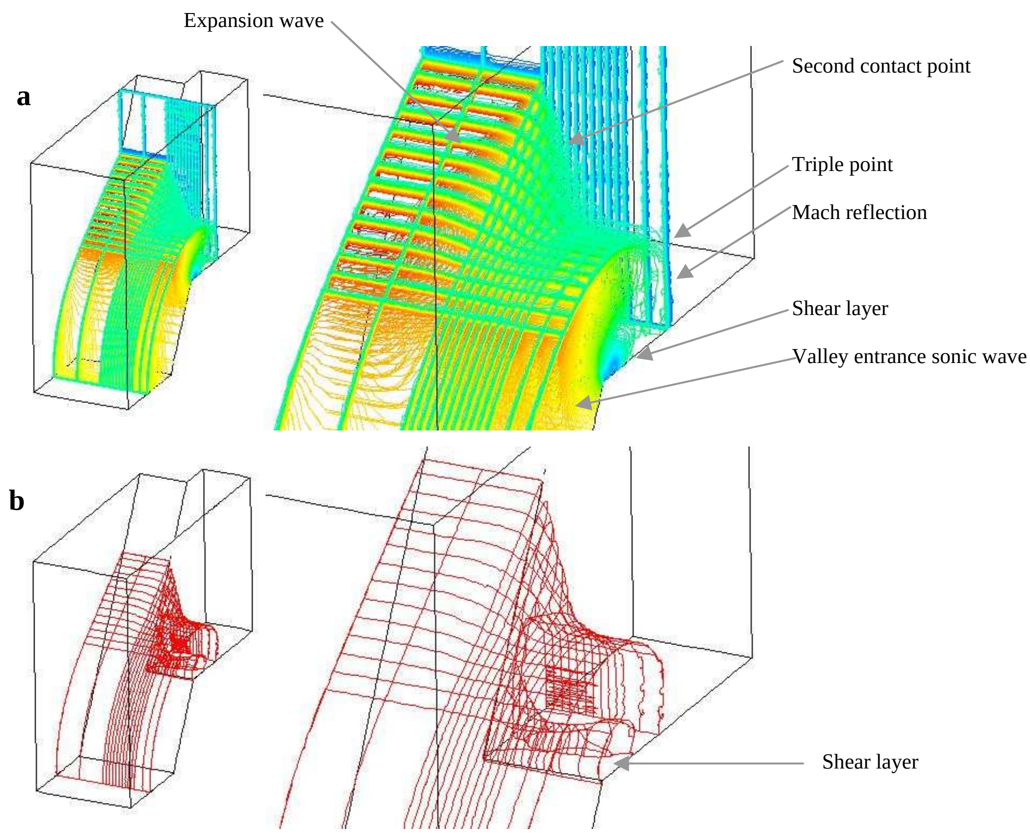

Figure 4.15: Isometric view of superimposed planes for rectangular valley, $\theta_w = 60^o$, $\theta_v = 0^o$. a) Entire flow field b) Secondary reflected wave

By using a NURBS modelling program, RHINOCEROS, a three-dimensional model of the resulting flow was generated. This was done by importing the planes generated in figure 4.4 into RHINOCEROS so the primary reflected wave surface could be generated. The same was done for the secondary reflected wave surface by importing the planes in figure 4.6. The shear layers, slip stream, incident shock wave and Mach stem were also generated using these planes. The back wave depicted in the model, shown in green, is the section of the incident wave which bows out into the downstream flow between the second contact point and the triple point. Figure 4.16 illustrates the three-dimensional model of the resulting wave structures for the rectangular valley, $\theta_w = 60^o$, $\theta_v = 0^o$.

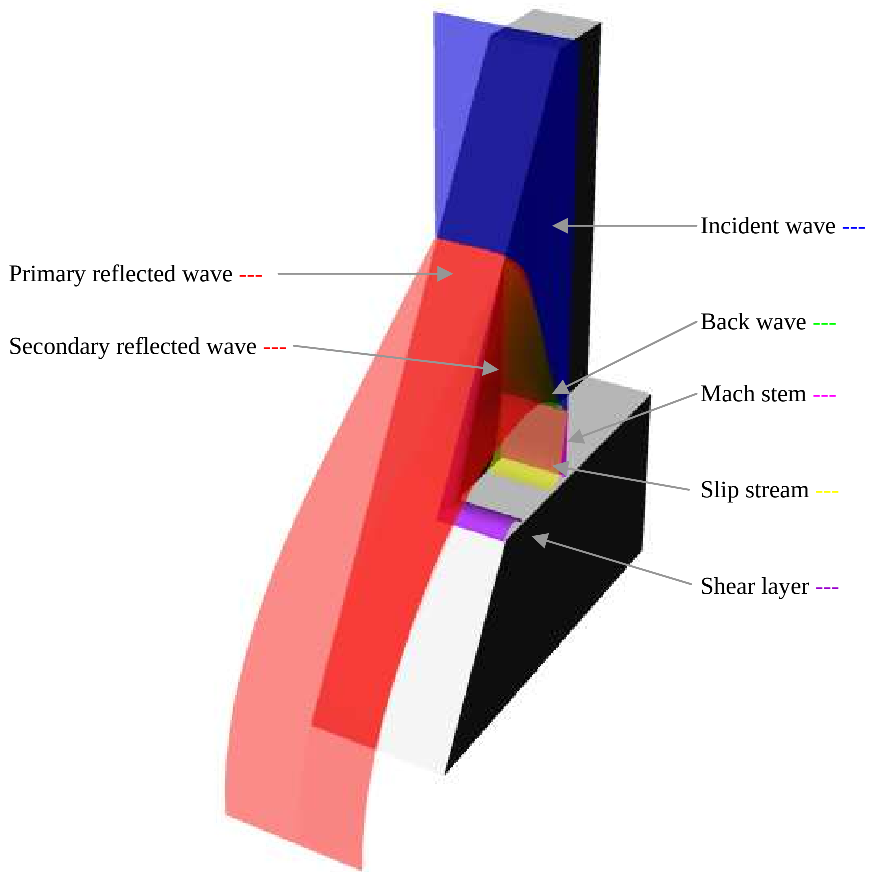

Figure 4.16: Three-dimensional NURBS model of rectangular valley, θ_w = 60°, θ_v = 0°.

4.3.2 Summary of results for various rectangular valley configurations

Seven more rectangular valley configurations were investigated. It was found that the general flow pattern for all rectangular valleys were very similar. The major difference found for the rectangular valleys with the same valley floor inclination but different wedge angles is the decreased effect of the sonic waves for the 70 degree wedge. The slight differences found in the numerous configurations due to the various valley floor inclination angles are discussed below. The images obtained through experimentation and numerical analysis for these seven rectangular valleys is presented in Appendix E1. The different configurations investigated included 15, 30 and 45 degree valley floor inclinations with a wedge angle of 60 degrees as well as 0, 15, 30 and 45 degree valley floor inclinations with a wedge angle of 70 degrees.

The images obtained experimentally at various time delays (similar to those in figure 4.1) for all rectangular configurations depicted regular reflection off the wedge and Mach reflection off the valley floor. The Mach reflection at a valley floor inclination of 45 degrees is very close to the transition point of regular reflection (verified by works of Ben-Dor 1991). It is also noted that the double sided tape used to protect the test section window of the shock tube against contact with the glass insert has partially blocked out the reflection off the valley floor for the 45 degree inclination. The sonic wave generated at the valley entrance is seen in all schlieren images, as well as the effect of the sonic wave from the first corner. The suggested three-dimensional wave structure is depicted in most sets of images, but not all due to the inherent variation of the optic system's sensitivity. The resulting Mach reflection slip stream is seen clearly in the images obtained for valley floor inclinations of 15 and 30 degrees. For the 70 degree wedge with a 0 degree valley floor inclination the presence of a shear layer at the valley entrance, as well as a second cascading down the valley wall, is seen in the schlieren images.

Numerical two-dimensional images taken at sequential time steps, similar to those in figure 4.3, confirm the regular reflection off the wedge surface and the Mach reflection off the valley floor found in the experimental images. The Mach stem becomes noticeably smaller at the larger valley floor inclinations. These images also depict a shear layer at the valley entrance which tends to increase in size as the incident wave advances down-steam. The shear layer is increasingly weaker at 30 and 45 degree valley floor inclinations. The sonic waves generated by both the wedge and valley entrance corners are depicted in the images and their influence on the flow increases as the flow advances. The weak slip stream is depicted in the images for all the configurations, but is seen very clearly for the 30 degree valley floor inclination.

Planes along the x axis were generated at a single time step, similar to figure 4.4, for all rectangular valley configurations. The regular reflection off the wedge surface is seen in the first couple of images. Mach reflection is seen to occur off the valley floor in the rest of the images. The Mach reflection occurs underneath the primary reflected wave which flows over into the valley for all configurations. The second contact point found in figure 4.4 is present for all rectangular valleys. The distance between the second contact point and the triple point is seen to decrease for all rectangular configurations the closer one moves to the symmetry plane until they coincide at a point close to the symmetry plane. The slight bowing of the incident wave between these two points is present in all rectangular valley configurations. The shear layer found at the valley entrance is confirmed for all configurations and travels the full width of the valley. The presence of the second shear layer cascading down the valley wall is seen in the images. The two sonic waves developed at the wedge and valley entrance corners are also depicted in the images. The slip stream is depicted in the last images and becomes stronger with increased valley floor inclinations.

Superimposed single level pressure contour plots generated at planes along the x axis, similar to figure 4.7 present the three-dimensional secondary reflected wave surface for all rectangular valley configurations. The Mach reflection is seen to occur over the full width of the valley. The surface becomes slightly distorted near the valley wall as it begins to climb up and along the valley wall, changing to regular reflection at the wedge surface. The Mach stem is seen to decrease in characteristic height at higher valley floor inclinations. This secondary wave pattern is present for all rectangular valley configurations, varying only slightly with increased valley floor inclination angles. The presence of the two shear layers is strongly depicted (merging at the valley entrance corner) in the images for the lower valley floor inclinations but at 30 degrees their presence is almost non-existent and at 45 degrees they are not seen at all. However, the shear layer is confirmed to be present for the 45 degree valley floor inclination previously but is extremely weak and therefore could not be established in the single level pressure contour plots.

Front views of planes generated along the z axis, similar to those in figure 4.11, illustrate the presence of the two shear layers for all rectangular valley configurations, including the weak shear layer for the 45 degree inclination. The presence of a Mach reflection in the x-y plane is present for all configurations, including a double triple point and two Mach stems. This second Mach reflection decreases in strength at higher valley floor inclinations. The planes also depict the sloping of the primary reflected wave as it flows over into the valley. The path of the second contact point (***A***) is illustrated for all configurations. The slope of the primary reflected wave as well as the second contact point path tend to become steeper the higher the valley floor inclination angle. The presence of an expansion wave is seen on the wedge surface for all configurations. By superimposing all these planes, as in figure 4.10 and 4.13 the surface is seen to be almost conical in nature near the valley wall, becoming tighter at higher valley floor inclinations.

To obtain a complete three-dimensional image of the reflected shock surfaces, planes along the x and z axes are superimposed, similar to figure 4.15a, for all rectangular valley configurations. The images developed for the different rectangular valleys are shown in figure 4.17. The incident shock, the primary reflected wave surface, the regular reflection off the wedge, the Mach reflection off the valley floor, the shear layer at the valley entrance and the sonic wave generated at the valley entrance can all be seen in the images. The images clearly illustrate the resulting three-dimensional wave structures. The figure also illustrates the slight differences with increasing valley floor inclination angles for both wedge angles. These include the decreased Mach stem height, less prominent shear layer and the tightening of the conical nature of the primary reflected surface.

The NURBS models for the rectangular valley generated for the 60 and 70 degree wedge angles with valley floor inclinations of 0 and 45 degrees are illustrated in figure 4.18.

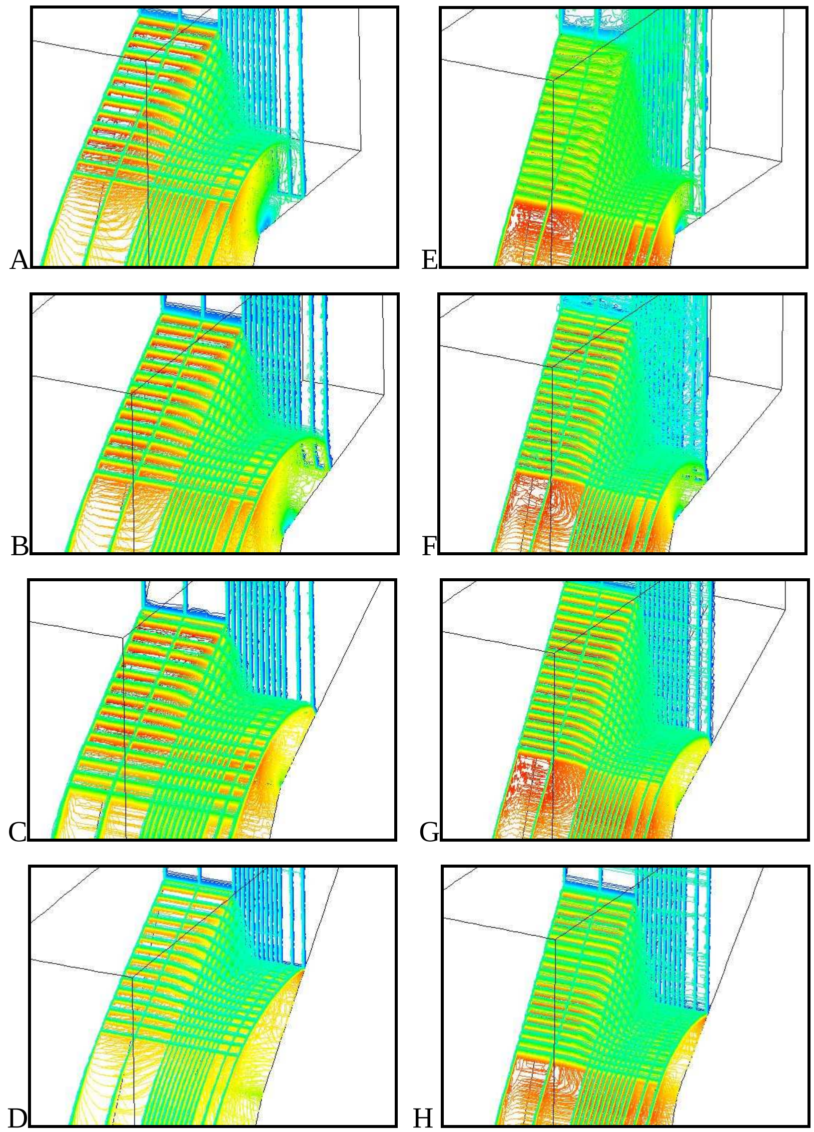

Figure 4.17: Isometric view of superimposed planes for rectangular valleys.

A) $\theta_w = 60º$, $\theta_v = 0º$ B) $\theta_w = 60º$, $\theta_v = 15º$ C) $\theta_w = 60º$, $\theta_v = 30º$ D) $\theta_w = 60º$, $\theta_v = 45º$

E) $\theta_w = 70º$, $\theta_v = 0º$ F) $\theta_w = 70º$, $\theta_v = 15º$ G) $\theta_w = 70º$, $\theta_v = 30º$ H) $\theta_w = 70º$, $\theta_v = 45º$

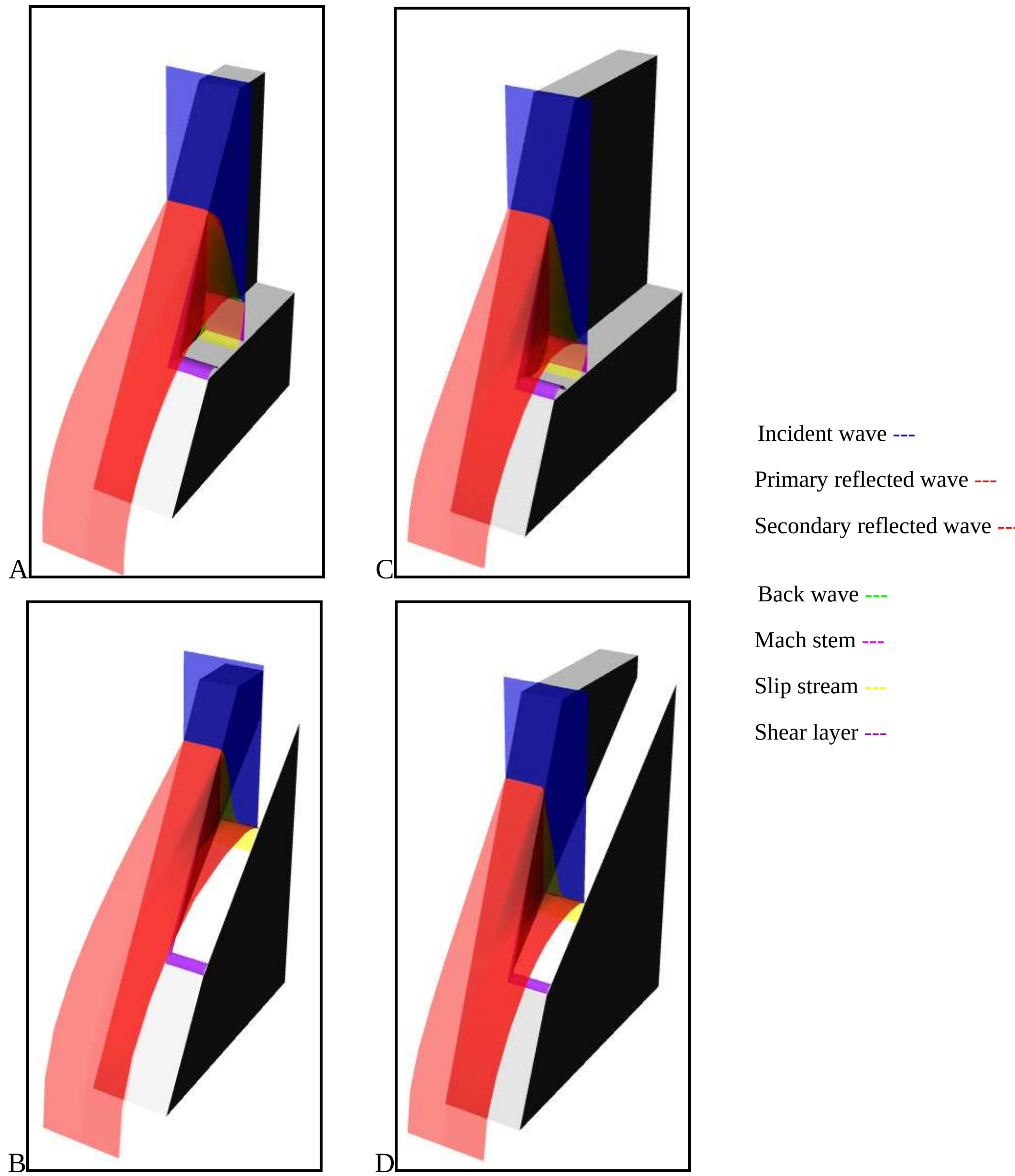

Figure 4.18 Three-dimensional NURBS model of rectangular valleys.

A) $\theta_w = 60^o$, $\theta_v = 0^o$ B) $\theta_w = 60^o$, $\theta_v = 45^o$ C) $\theta_w = 70^o$, $\theta_v = 0^o$ D) $\theta_w = 70^o$, $\theta_v = 45^o$

4.4 Triangular valley results

4.4.1 Triangular valley, $\theta_w = 60°$, $\theta_v = 0°$

Schlieren images are presented in figure 4.19, taken at sequential time delays. There is no glass piece incorporated into the triangular valley due to their angular geometry. Therefore one can not determine the reflection off the valley floor as the opaque manufacturing material blocks out this reflection. The reflection off the wedge is regular, as expected, and is seen in all schlieren images. The reflected wave from the reflection off the valley floor is depicted in the images upstream of the wedge. The suggested three-dimensional surface is seen in all images, due to the different positions of the two reflected waves. The effect of the first corner is seen throughout the images, and has greater influence on the reflection as the incident shock advances downstream. A sonic wave generated at the valley entrance point is present in the images.

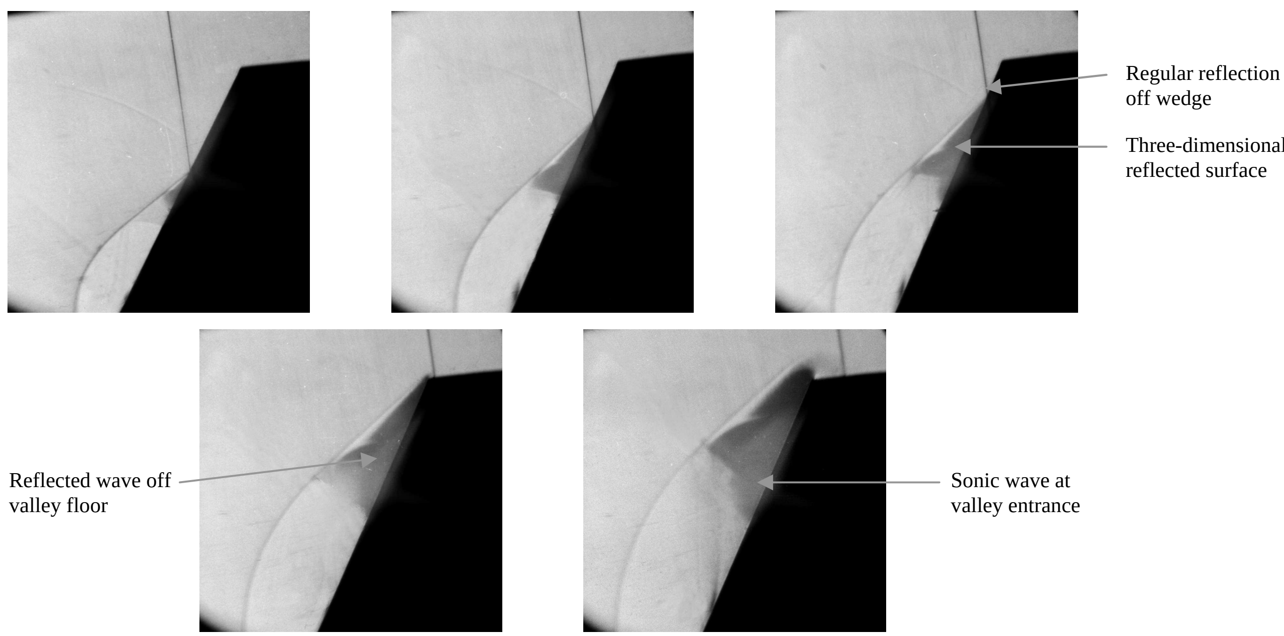

Figure 4.19: Schlieren images for triangular valley, $\theta_w = 60°$, $\theta_v = 0°$, at time delay 1700µs, 1725µs, 1750µs, 1775µs, and 1800µs respectively.

Numerical two-dimensional images were produced from the three-dimensional solution by taking planes which were just inside the walls of the test piece, i.e. at 0mm and 75mm along the x-axis, shown in figure 4.20. These planes were used in validation of the experimental results for all triangular valleys. The two-dimensional images were taken at sequential time steps, allowing the reflection off the wedge and valley floor surfaces to be analysed and compared to the schlieren images obtained experimentally. The reflection off the wedge is regular reflection and off the valley floor at the plane of symmetry is Mach reflection. The regular reflection off the wedge and the resulting reflected wave from the valley floor compare directly with the experimental results. A shear layer at the valley entrance point can be depicted in these images. As the incident shock advances downstream both the Mach stem and shear layer tend to increase in characteristic height and size. The influence of the sonic waves generated by both the wedge and valley entrance corners can also be depicted in these images. A slip stream, generated at the symmetry plane, can also be seen in the images.

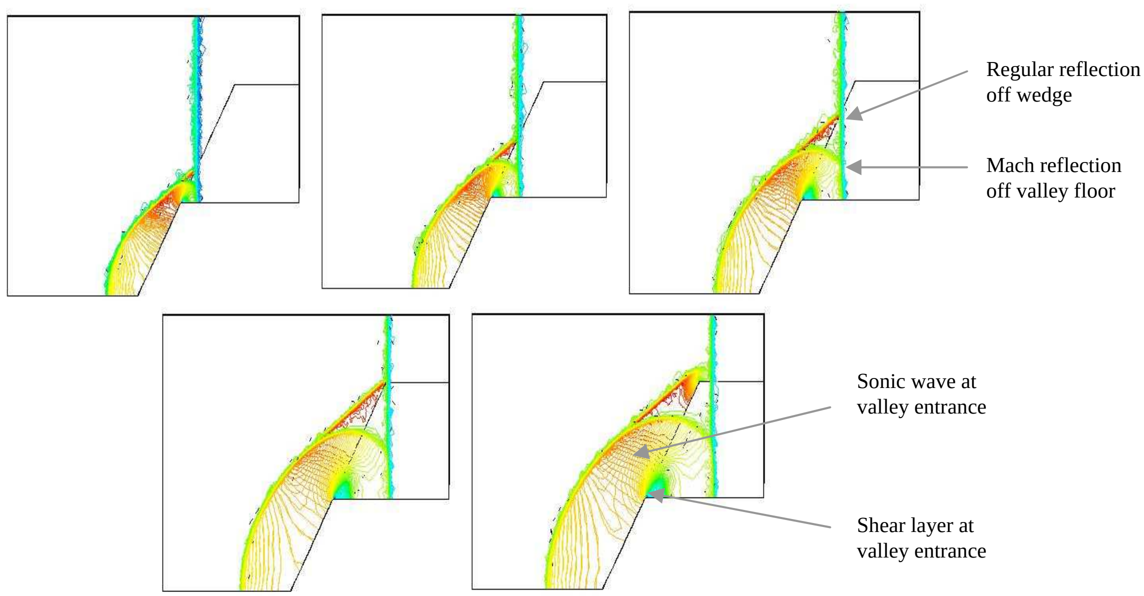

Figure 4.20: Sequential density contour plots for triangular valley, $\theta_w = 60°$, $\theta_v = 0°$.

In order to determine the geometric structure of the three-dimensional reflected shock surfaces, planes along the x axis were taken at a single time step. The planes depict how the wave structures change across the width of the test piece. The planes starting at 0mm (wedge wall) and ending at 75mm (symmetry plane) can be seen in figure 4.21. The regular reflection off the wedge is seen in the first two images. As the incident shock interacts with the valley, Mach reflection occurs off the valley floor. The regular reflected surface off the wedge and the Mach reflected surface off the valley floor merge to form a single reflected surface referred to as the primary reflected surface. The Mach stem is seen to increase in characteristic height as the reflection moves down the valley wall. The shear layer found in figure 4.20 is seen to cascade down the valley entrance wall, increasing in strength towards the symmetry plane. The two sonic waves developed at the wedge corner and valley entrance are depicted in the images. The slip stream can also be depicted in the planes close to the symmetry plane.

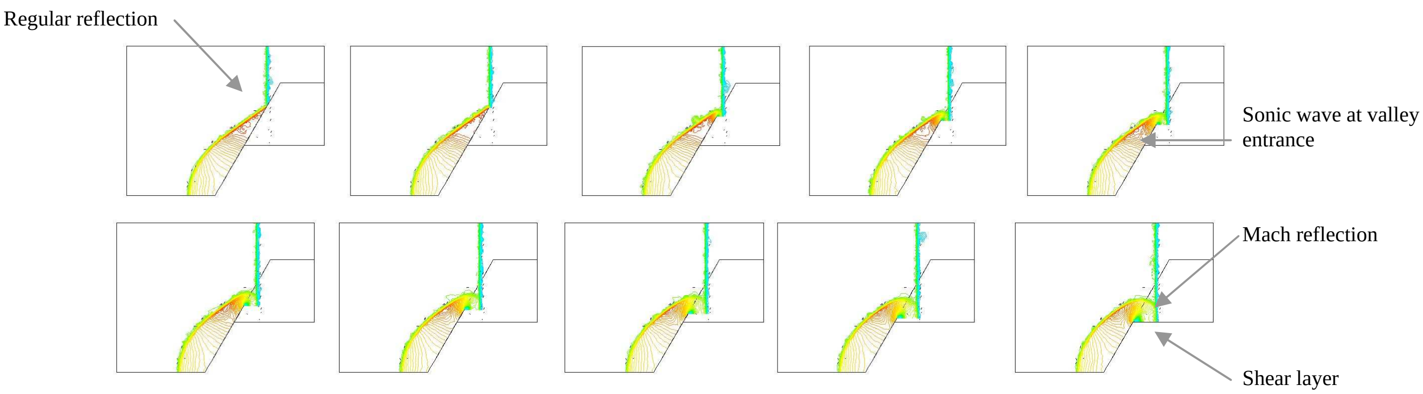

Figure 4.21: Density contour plots for triangular valley, $\theta_w = 60^o$, $\theta_v = 0^o$, taken in the y-z plane at x = 0mm, 25mm, 35mm, 45mm, 50mm, 55mm, 60mm, 65mm, 70mm and 75mm respectively.

On closer inspection of the three-dimensional numerical solution, a weak secondary reflected wave was found underneath the primary reflection. By taking planes across the x axis and generating single level pressure contour plots, the secondary reflection could be better understood. Figure 4.22 illustrates these various pressure contour plots. The reflection tends to initially wrap over the shear layer as one moves down the valley entrance wall. At a point close to the symmetry plane the reflection then moves over the valley surface, becoming Mach reflection. Figure 4.23 is a superimposition of the planes in figure 4.22, and illustrates the three-dimensional geometry of the secondary reflected wave. The shear layer formed down the valley entrance wall is also depicted in the images.

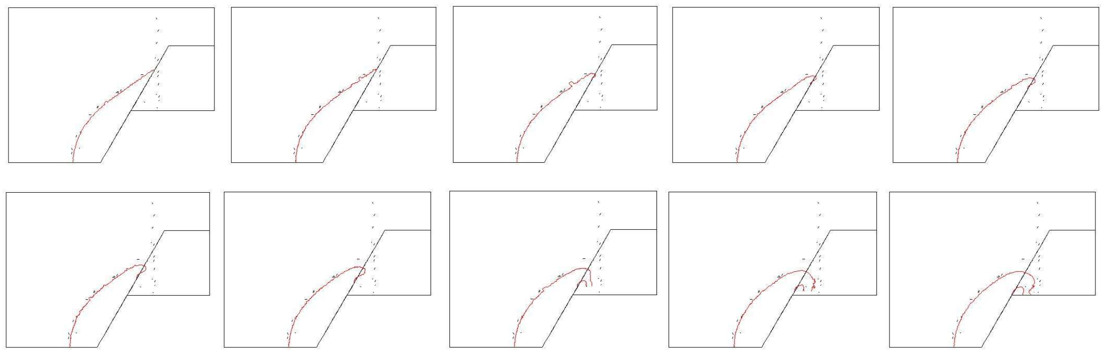

Figure 4.22: Pressure contour plots (single level) of secondary reflected wave for triangular valley, θ_w = 60º, θ_v = 0º, taken in the y-z plane at x = 0mm, 25mm, 35mm, 45mm, 50mm, 55mm, 60mm, 65mm, 70mm and 75mm respectively.

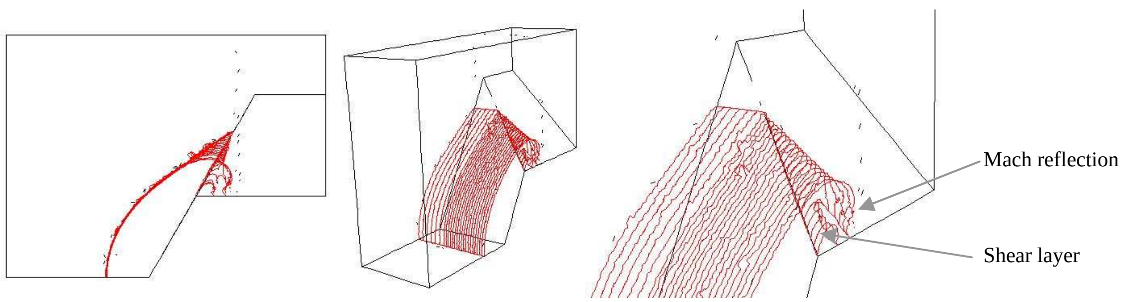

Figure 4.23: Superimposed pressure contour plots (single level) of secondary reflected wave for triangular valley, θ_w = 60º, θ_v = 0º.

In order to develop a complete three-dimensional understanding of the resulting wave structures, planes along the z axis were generated. Isometric and front views of these planes are shown in figures 4.24 and 4.26 respectively. The images depict the shear layer cascading down the valley entrance wall. One can also see an expansion wave on the wedge surface. The planes also depicted the sloping of the primary reflected wave as it propagates into the valley. The further downstream, the steeper the surface becomes. The second last image in figure 4.26 illustrates the path of the triple point of the Mach reflection occurring off the valley floor. By superimposing all the planes generated along the z axis, figure 4.25 illustrates an isometric view of the reflected wave structure. A very weak reflection from the symmetry plane can be seen in the figure. This reflection coincides with the very weak, but present, secondary reflected wave surface.

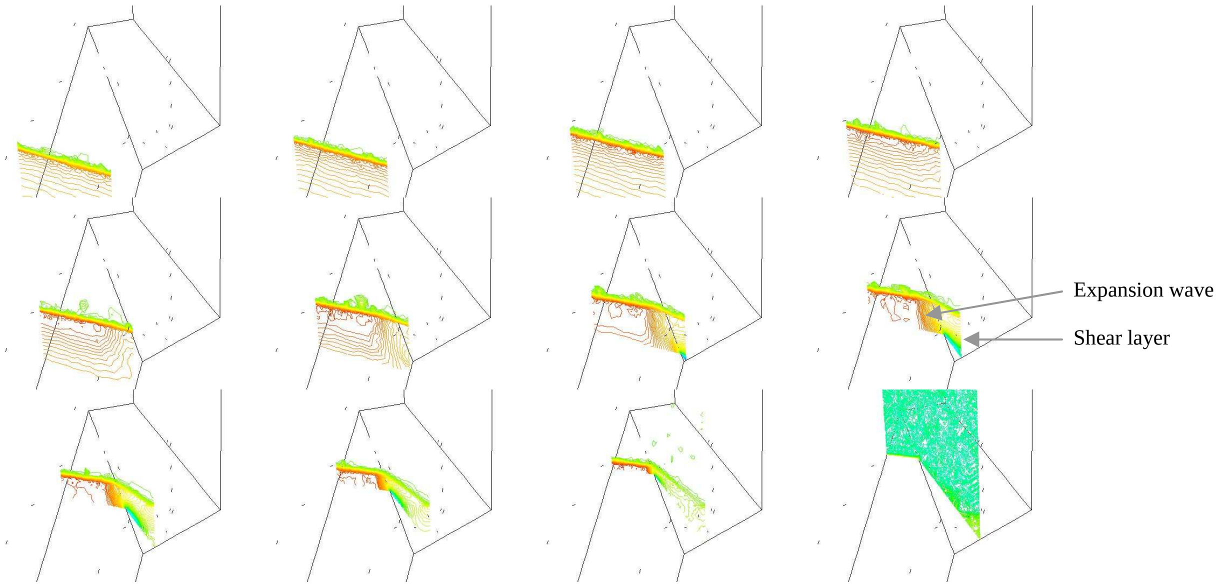

Figure 4.24: Isometric views of sequential density contour plots for triangular valley, θ_w = 60º, θ_v = 0º, taken in the x-y in steps of 5mm along the z axis.

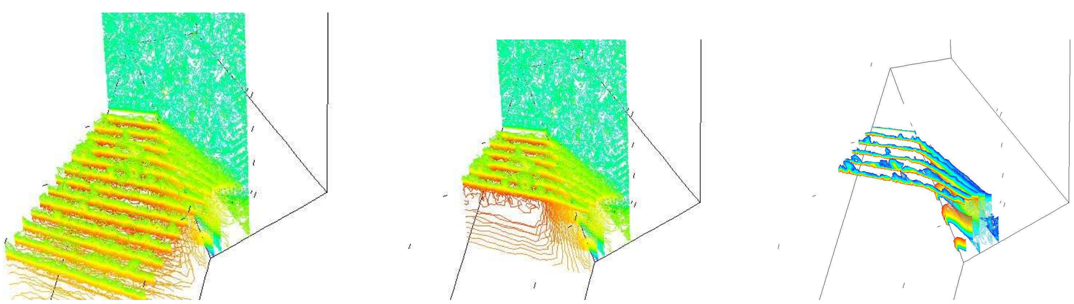

Figure 4.25: Isometric view of superimposed density contour plots for triangular valley, θ_w = 60º, θ_v = 0º, taken in the x-y plane.

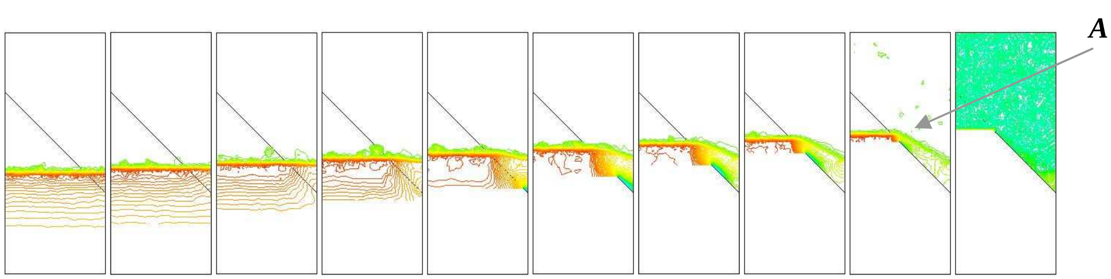

Figure 4.26: Sequential density contour plots for triangular valley, θ_w = 60º, θ_v = 0º, taken in the x-y plane in steps of 5mm along the z axis.

Figure 4.27 represents a couple of images enlarged from figure 4.26 for better clarity of the problem. Figure 4.28 is a front view of the superimposition of the planes illustrated in figure 4.26, and depicts the sloping of the primary reflected wave surface.

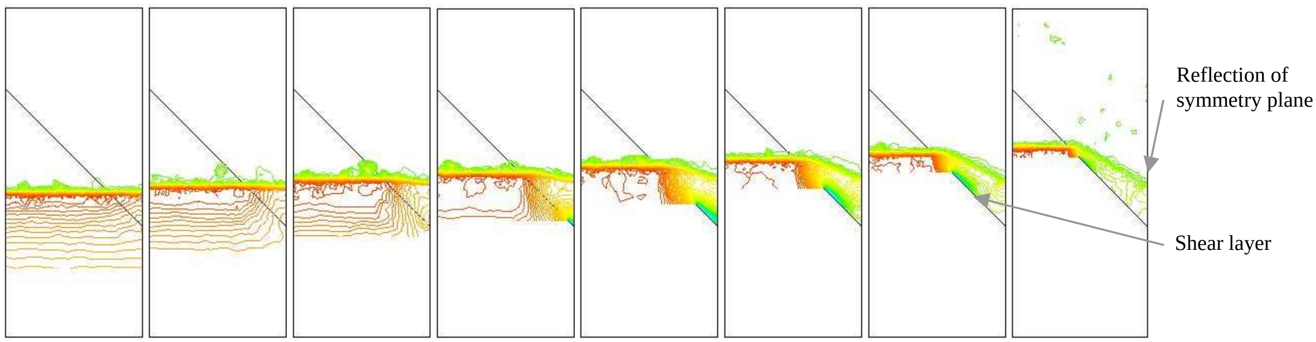

Figure 4.27: Enlarged sequential density contour plots for triangular valley, $\theta_w = 60^o$, $\theta_v = 0^o$, taken in the x-y in steps of 5mm along the z axis.

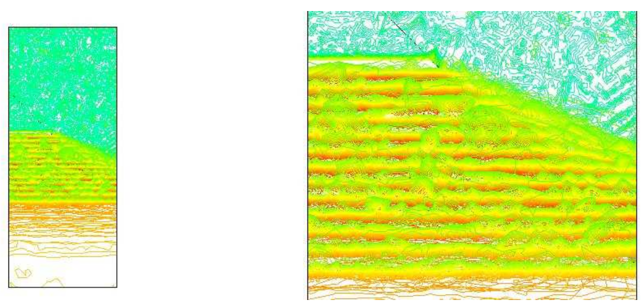

Figure 4.28: Superimposed density contour plots for triangular valley, $\theta_w = 60^o$, $\theta_v = 0^o$, taken in the x-y plane.

Figure 4.29 represent a filled density contour plot of a plane just offset from the symmetry plane. The figure illustrates the presence of the shear layer at the valley entrance wall.

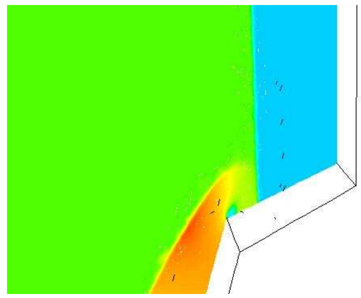

Figure 4.29: Filled density contour plot of plane in y-z plane for triangular valley, θ_w = 60º, θ_v = 0º, illustrating shear layer.

To obtain a complete three-dimensional image of the reflected shock surfaces, planes along the x and z axes are superimposed, as shown in figure 4.30a. The incident shock, the primary reflected wave, the regular reflection off the wedge, the Mach reflection off the valley floor, the shear layer at the valley entrance wall and the sonic wave at the valley entrance can point all be seen in the figure. However, the secondary reflected wave is covered by the primary reflected wave surface. To illustrate the three-dimensional surface of the secondary reflected wave, figure 4.30b is presented.

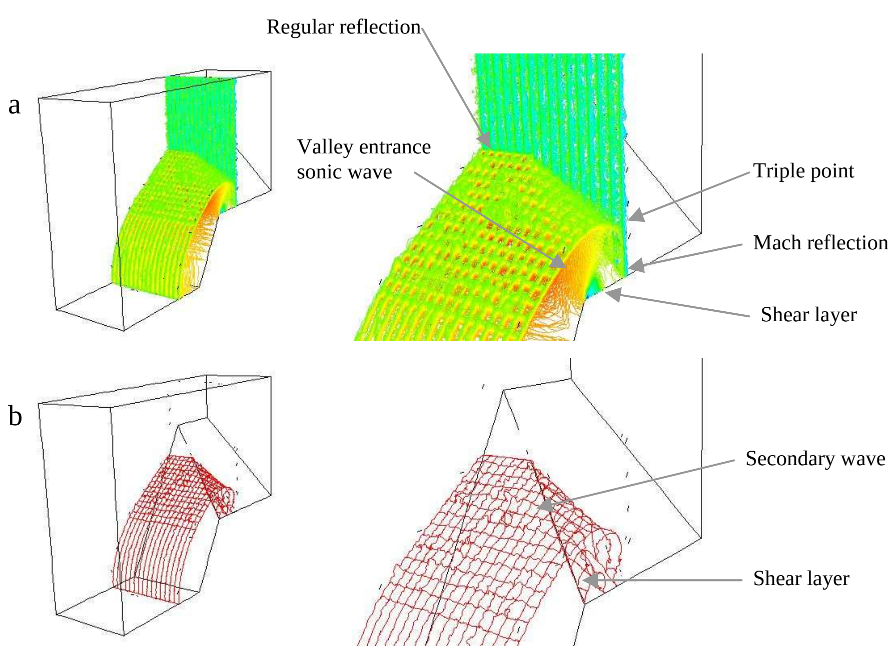

Figure 30: Isometric view of superimposed planes for triangular valley, θ_w = 60º, θ_v = 0º.

a) Entire flow field b) Secondary reflected wave

By using a NURBS modelling program, RHINOCEROS, a three-dimensional model of the resulting flow was generated. This was done by importing the planes generated in figure 4.21 into RHINOCEROS so the primary reflected wave surface could be generated. The same was done for the secondary reflected wave surface by importing the planes in figure 4.22. The shear layer, slip stream, incident shock wave and Mach stem were also generated using these planes. Figure 4.31 illustrates the three-dimensional model of the resulting wave structures for the triangular valley, $\theta_w = 60^o$, $\theta_v = 0^o$.

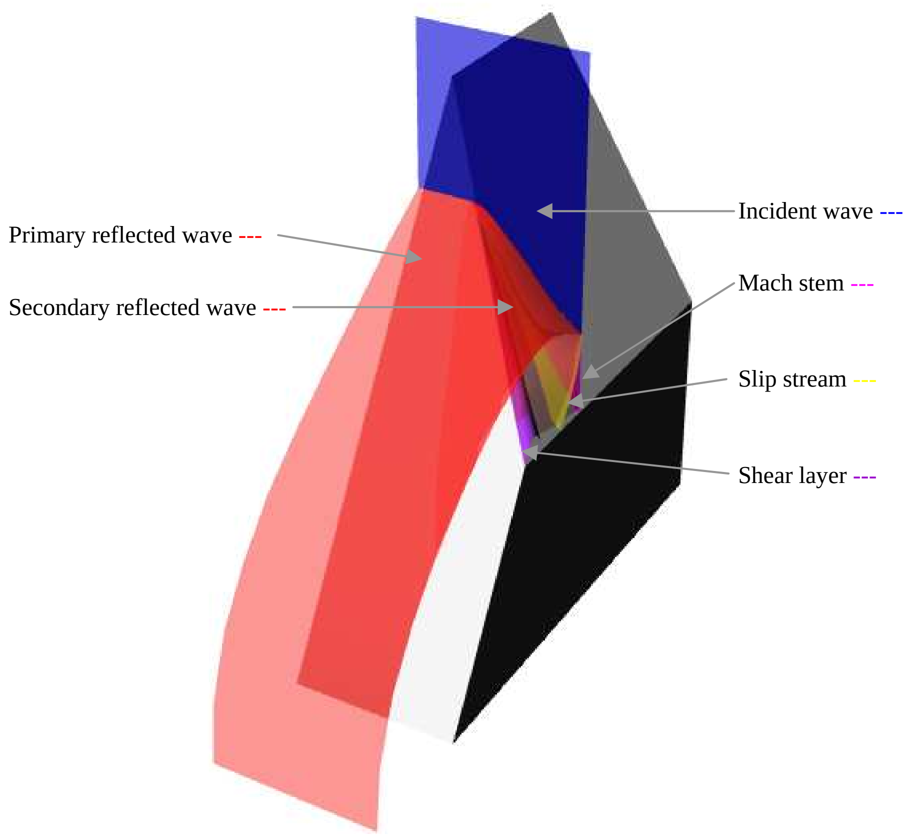

Figure 4.31: Three-dimensional NURBS model of triangular valley, $\theta_w = 60^o$, $\theta_v = 0^o$.

4.4.2 Summary of results for various triangular valley configurations

Seven more triangular valley configurations were investigated. It was found that the general flow pattern for all triangular valleys were very similar. The major difference found for the triangular valleys with the same valley floor inclination but different wedge angles is the decreased effect of the sonic waves for the 70 degree wedge. The slight differences found in the numerous configurations due to the various valley floor inclination angles are discussed below. The images obtained through experimentation and numerical analysis for these seven triangular valleys is presented in Appendix E2. The different configurations investigated included 15, 30 and 45 degree valley floor inclinations with a wedge angle of 60 degrees as well as 0, 15, 30 and 45 degree valley floor inclinations with a wedge angle of 70 degrees.

Schlieren images taken at sequential time delays were obtained for all triangular valley configurations, similar to those presented in figure 4.19. The reflection off the wedge surface is regular for all triangular valleys. Once again the reflection off the valley could not be seen due to the opaque nature of the manufacturing material. However, the resulting reflected wave from this reflection could be seen upstream of the wedge. The reflection for the 70 degree wedge with a valley floor inclination of 45 degrees was very weak in the images, but nether the less present. The suggested three-dimensional surface is seen in the images for all triangular configurations except for the 70 degree wedge with a 45 degree valley floor inclination. The effect of the first corner is seen throughout the images, having greater influence on the reflection as the incident shock advances downstream. A sonic wave generated at the valley entrance point is also present in the images for all configurations except for the 70 degree wedge with a 45 degree valley floor inclination. The discrepancy in the images obtained for 70 degree wedge with a 45 degree valley floor inclination was due to the fact that the optic system was not sensitive enough to pick up the weak reflection pattern.

Numerical two-dimensional images taken at sequential time steps, similar to those in figure 4.20, were obtained for all triangular valley configurations. The reflection off the wedge surface is regular reflection and off the valley floor at the plane of symmetry is Mach reflection. The regular reflection and resulting reflected wave from the valley floor reflection compare directly with the experimental results for all triangular configurations. A shear layer at the valley entrance point is depicted in the images for all configurations but is weaker at higher valley floor inclinations. As the incident wave advances downstream both the shear layer and Mach stem increase in characteristic height and size. The Mach stem is noticeably smaller for higher valley floor inclination angles. The influence of the sonic waves generated at both the wedge and valley entrance corners are also depicted in the images for all triangular configurations, however the sonic wave at the valley entrance is noticeably weaker for a 45 degree valley floor inclination. A slip stream at the symmetry plane is also seen in the images for all triangular configurations as is much stronger at higher valley floor inclination angles.

Planes along the x axis were generated at a single time step for all triangular valley configurations, similar to figure 4.21. The regular reflection off the wedge is seen in the first images for all configurations. As the incident shock interacts with the valley, Mach reflection occurs off the valley floor, depicted in the rest of the images. The regular reflected surface off the wedge and the Mach reflected surface off the valley floor again merge to form a single surface referred to as the primary reflected surface. The Mach stem is seen to increase in characteristic height as the planes move closer to the symmetry plane for all triangular configurations. The shear layer is found to cascade down the valley entrance wall for all configurations and is again noted to be weaker for higher valley floor inclination angles. The slip stream can also be depicted in the planes close to the symmetry plane for all configurations. Unlike the first triangular valley case, these images obtained for all other triangular valley configurations show a strong presence of the secondary reflected wave.

Single level pressure contour plots generated at planes along the x axis are superimposed to present the three-dimensional secondary reflected wave surface for all triangular valley configurations, similar to figure 4.23. The secondary reflected wave occurs underneath the primary reflected wave surface for all triangular configurations. The images depict the reflected surface initially wrapping over the shear layer as one moves down the valley entrance wall. At a point close to the symmetry plane the reflection, in regular form, then moves over the valley surface, becoming Mach reflection at a certain point. This pattern is similar for all configurations. The shear layer formed down the valley entrance wall is also depicted in the images, except for the 45 degree valley floor inclination. This is only due to the fact that the shear layer is extremely weak for this configuration and could not be picked up using single level pressure contour plots.

Front views of planes generated along the z axis were developed for all triangular valley configurations, similar to those in figure 4.26. The images depict the shear layer cascading down the valley entrance wall for all triangular configurations, including the weak shear layer for the 45 degree valley floor inclination. An expansion wave on the wedge surface is seen for all configurations. The images also depict the sloping of the primary reflected wave structure as well as the path (***A***) of the triple point of the Mach reflection off the valley floor. At the point where the primary reflection coincides with the symmetry plane, the reflected wave surface is perpendicular to this plane, illustrating that the primary reflected surface flattens out near the symmetry plane. A reflection off the symmetry plane is also depicted in the images for all configurations, coinciding with the secondary reflected wave geometry close to the symmetry plane. By superimposing all the planes for each configuration an isometric view of the reflected wave pattern is developed and presents, in more detail, the secondary reflected wave close to the symmetry plane.

To obtain a complete three-dimensional image of the reflected shock surfaces for all triangular valley configurations, planes along the x and z axes are superimposed, as shown in figure 4.32. The incident shock, the primary reflected wave surface, the regular reflection off the wedge, the Mach reflection off the valley floor, the shear layer at the valley entrance and the sonic wave at the valley entrance can all be seen in the figure. The figure also illustrates the differences in the resulting wave structures for different configuration. The increase in valley floor inclination angle decreased the Mach stem height of the Mach reflection close to the symmetry plane, made the resulting slip stream more prominent, decreased the strength of the corner signal at the valley sentence point and decreased the strength of the shear layer cascading down the valley entrance wall.

The NURBS models for the triangular valleys generated for the 60 and 70 degree wedge angles with valley floor inclinations of 0 and 45 degrees are illustrated in figure 4.33.

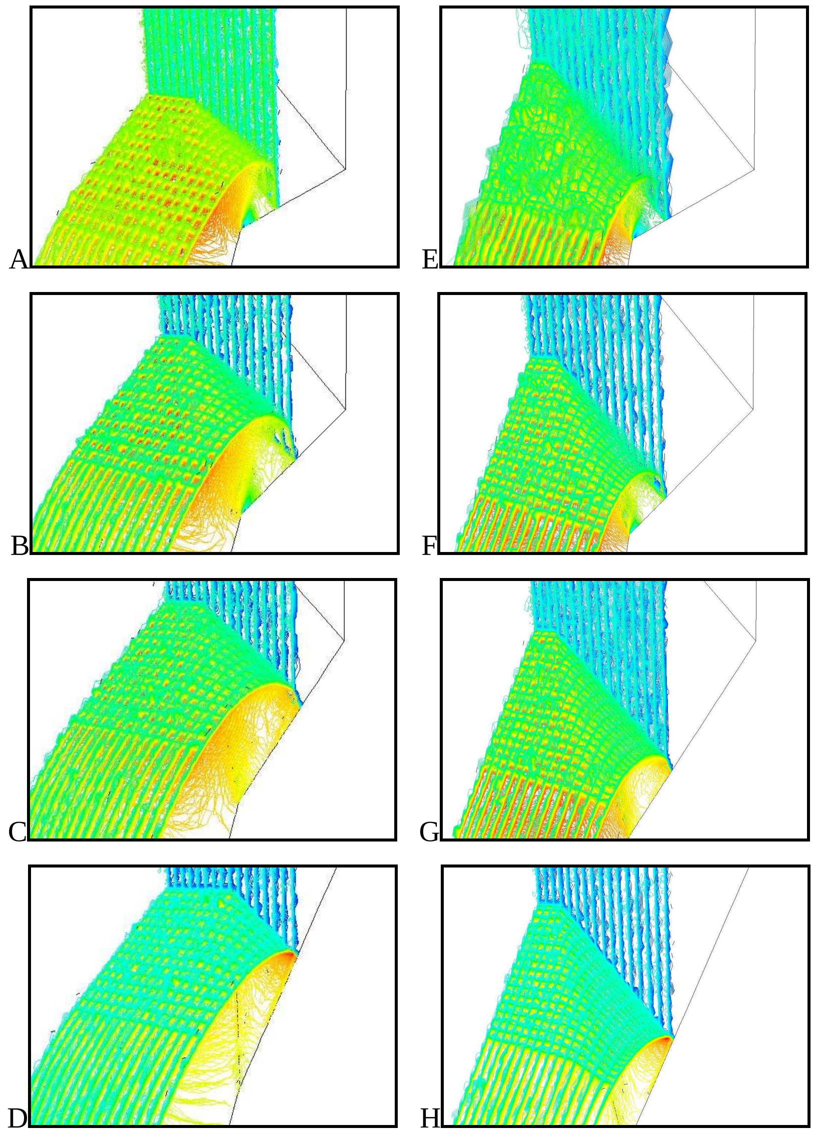

Figure 4.32: Isometric view of superimposed planes for triangular valleys.

A) $\theta_w = 60^o$, $\theta_v = 0^o$ B) $\theta_w = 60^o$, $\theta_v = 15^o$ C) $\theta_w = 60^o$, $\theta_v = 30^o$ D) $\theta_w = 60^o$, $\theta_v = 45^o$

E) $\theta_w = 70^o$, $\theta_v = 0^o$ F) $\theta_w = 70^o$, $\theta_v = 15^o$ G) $\theta_w = 70^o$, $\theta_v = 30^o$ H) $\theta_w = 70^o$, $\theta_v = 45^o$

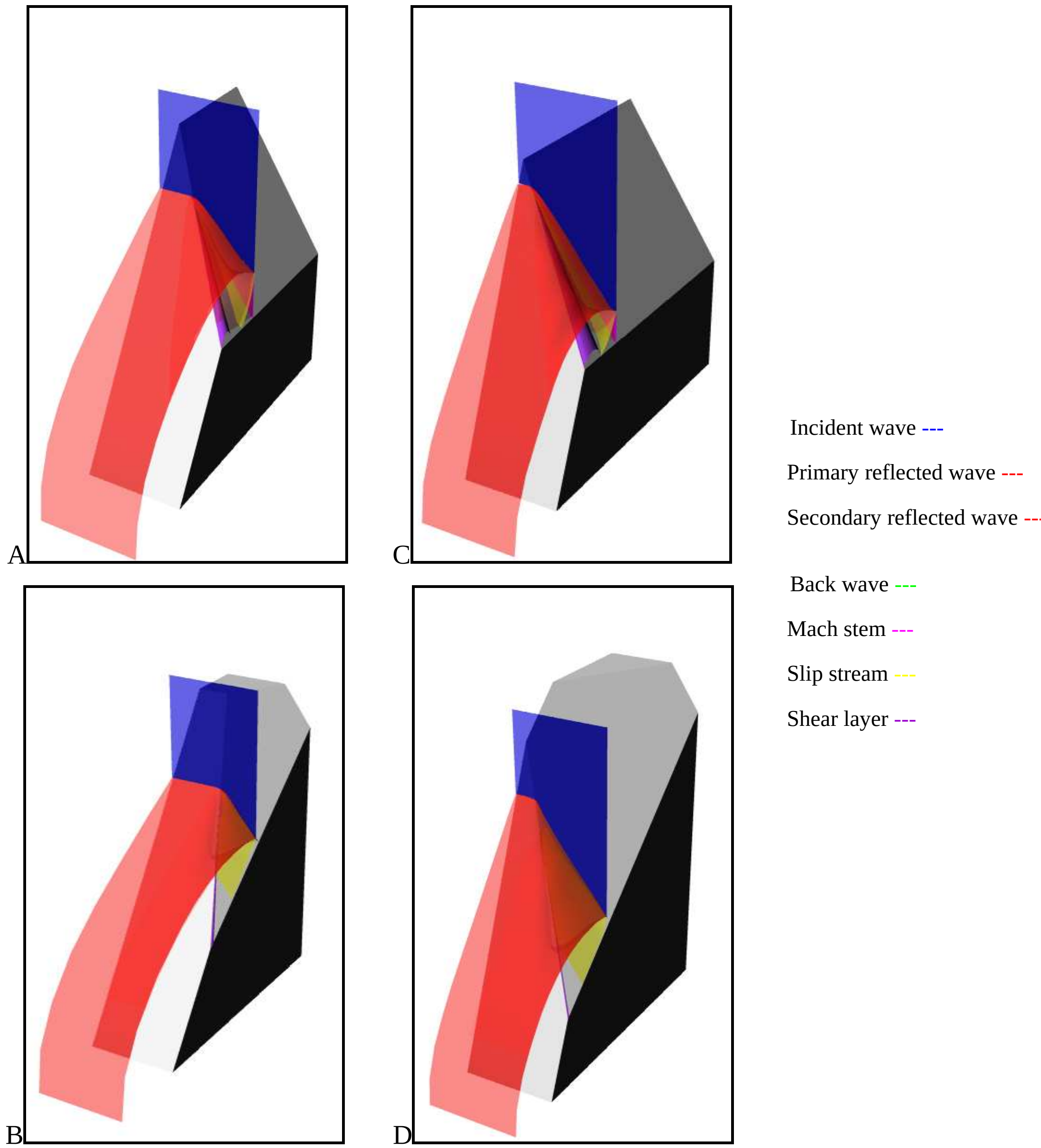

Figure 4.33 Three-dimensional NURBS model of triangular valleys.

A) $\theta_w = 60^o, \theta_v = 0^o$ B) $\theta_w = 60^o, \theta_v = 45^o$ C) $\theta_w = 70^o, \theta_v = 0^o$ D) $\theta_w = 70^o, \theta_v = 45^o$

4.5 Parabolic valley results

4.5.1 Parabolic valley, a = 0.04

Schlieren images are presented in figure 4.34, taken at sequential time delays. The reflection off the wedge is regular, as expected. The reflection off the valley floor is blocked out in all images for the parabolic valleys due to the opaque nature of the manufacturing material. However, the reflected wave from the valley floor reflection can be seen upstream of the wedge. The suggested three-dimensional wave structure can also be depicted from the schlieren images, due to the different positions of the two reflected waves. A sonic wave generated at the valley entrance can be seen in all schlieren images, as well as the effect of the sonic wave from the first corner. The further downstream the incident shock moves, the greater the influence of the sonic wave becomes on the reflected shock.

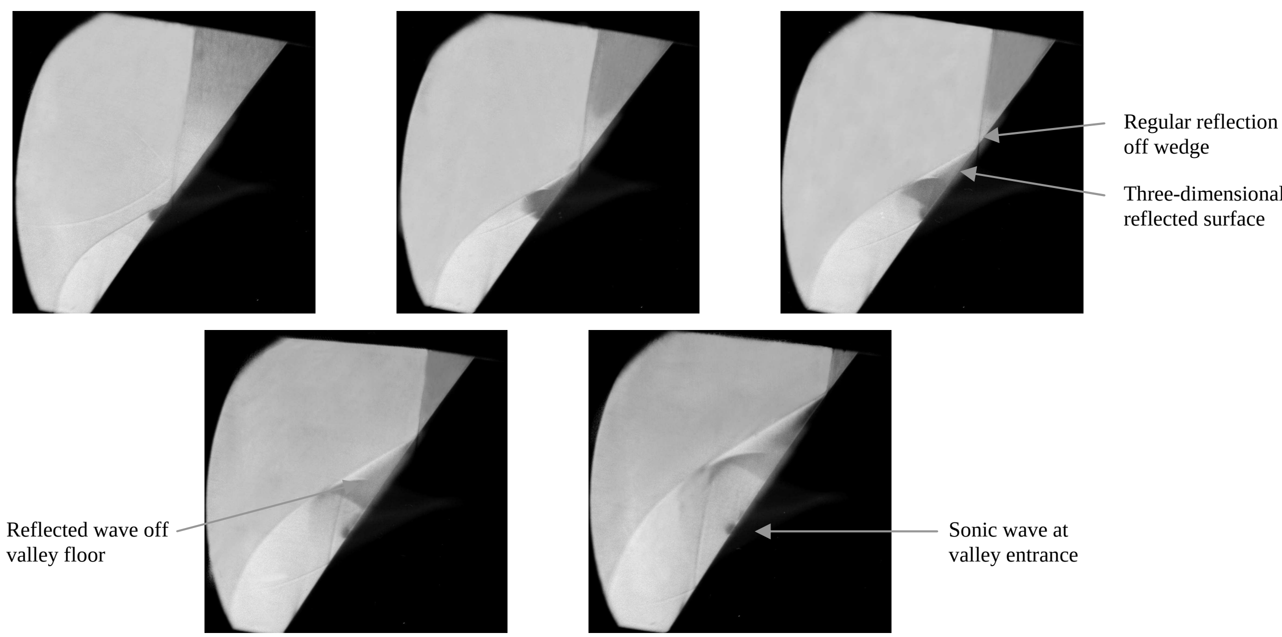

Figure 4.34: Schlieren images for parabolic valley, a = 0.04, at time delay 1650µs, 1675µs, 1700µs, 1725µs, and 1750µs respectively.

Numerical two-dimensional images were produced from the three-dimensional solution by taking planes at 0mm and 75mm along the x axis. These planes were used in validation of the experimental results for all parabolic valleys. The two-dimensional images were taken at sequential time steps, allowing direct comparison of the reflection off the wedge and valley surfaces to the schlieren images. The regular reflection off the wedge surface and the reflected wave from the valley floor can be depicted in the images presented in figure 4.35, and compare directly with the experimental results. The reflected wave from the wedge surface is also found at the plane of symmetry (x = 75mm) and is referred to as the primary reflected wave. The reflection off the valley surface at the plane of symmetry is Mach reflection, and is referred to as the secondary reflected wave. A shear layer at the symmetry plane can also be depicted in these images at the valley entrance point. The reflected Mach wave off the valley floor forms a semi-circle configuration and makes contact with the valley floor just before the shear layer. From the initial time steps, the presence of a second contact point from the primary reflected wave, above the triple point is depicted. As the incident shock wave advances downstream, this second contact point tends to move down the incident shock and coincide with the triple point. Further analysis found that this second contact point then moves along the secondary reflected wave as the incident shock propagates further downstream. The effect of the first and second corners on the reflected wave can be seen as the incident shock advances downstream. The slip stream of the Mach reflection at the plane of symmetry can be seen in the last image.

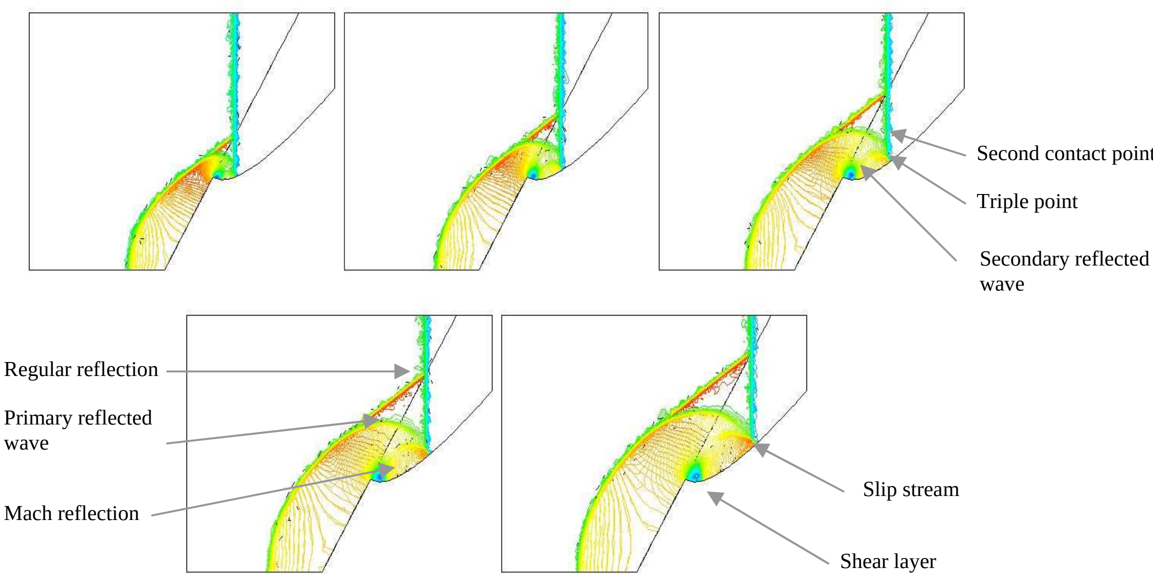

Figure 4.35: Sequential density contour plots for parabolic valley, a = 0.04.

In order to determine the three-dimensional reflected shock surfaces, planes along the x axis were taken at a single time step. The planes depict how the wave structures change across the width of the test piece. The images can be seen in figure 4.36. The regular reflection off the wedge surface can be seen in the first three images. As the incident wave interacts with the parabolic valley, regular reflection occurs off the valley floor. As the planes move closer to the symmetry plane, Mach reflection occurs off the valley floor underneath the primary reflected surface. The Mach stem's characteristic height then increases as it nears closer to the symmetry plane. The presence of the second contact point on the incident wave is found as the primary reflected wave flows over in to the valley. The second contact point can be seen in the last five images, and moves towards the triple point as the planes move closer to the symmetry plane. The Mach reflection found at the plane of symmetry in figure 4.35 can also be seen in the last four images of figure 4.36. The shear layer, found in figure 4.35, cascades down the valley entrance as the planes move along the x axis. The presence of the slip stream is also apparent in the last few images.

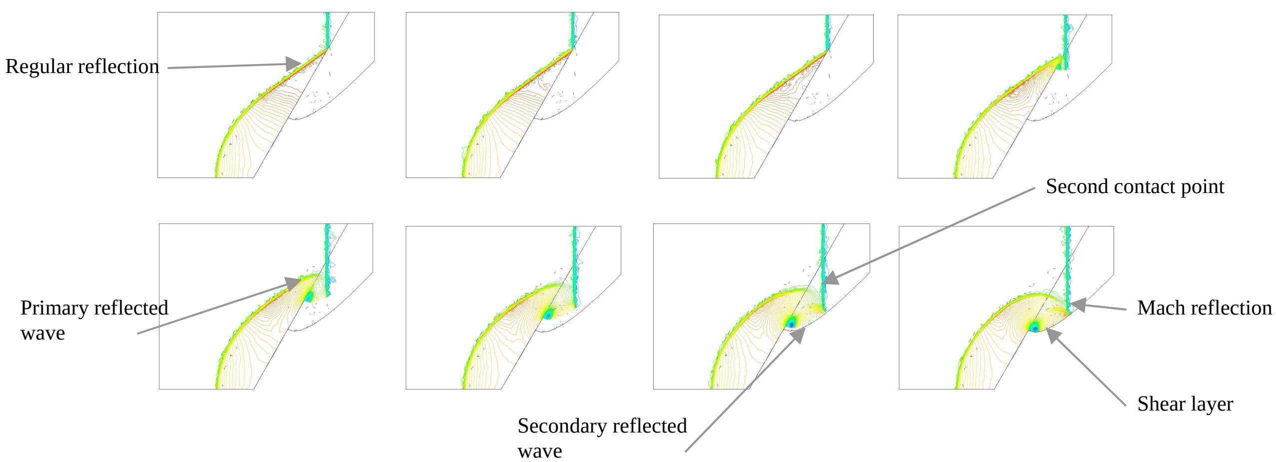

Figure 4.36: Density contour plots for parabolic valley, a = 0.04, taken in the y-z plane at x = 0mm, 15mm, 25mm, 35mm, 45mm, 55mm, 65mm, 75mm, respectively.

To determine the three-dimensional wave structure of the reflection off the valley floor (secondary reflected wave), single level pressure contour plots were created. Figure 4.37 was developed by superimposing several planes across the x and z axes. The figure validates the dissipation of the Mach reflection, and transition to regular reflection as the reflected wave climbs up and along the valley entrance wall. The shear layer cascading down the valley entrance wall is also seen in these images. Once the Mach reflected wave has terminated, the reflection point then travels up along the valley entrance until it meets the regular reflection at the wedge surface.

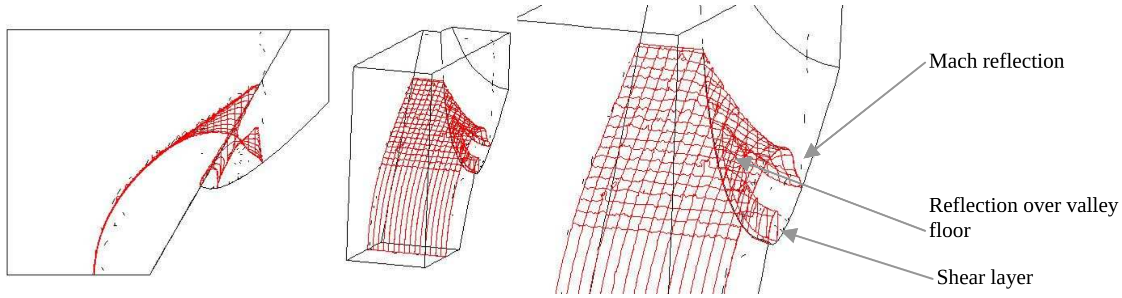

Figure 4.37: Superimposed pressure contour plots (single level) of secondary reflected wave for parabolic valley, a = 0.04.

To develop a complete three-dimensional understanding of the resulting wave structures, planes along the z axis were generated. Front views of these planes are shown in figure 4.38. Figure 4.39 enlarges the latter images in figure 4.38 to show more detail in the reflection pattern. The sequential planes clearly illustrate the shear layer formed at the valley entrance wall. The planes also illustrate that the curvature of the primary reflected surface tends to become steeper the closer the plane is to the incident shock. A reflection off the plane of symmetry is also depicted in the images. This reflection is the Mach reflection off the valley floor, and illustrates the reflection geometry in the x-y plane. An expansion wave over the wedge surface is seen throughout the images. It is seen that the primary reflected wave is perpendicular to the plane of symmetry, at this plane. The point where the primary reflected wave touches the plane of symmetry tends to move downwards as the planes advance up the z axis. The multiple x-y planes are superimposed to create a three-dimensional image of the reflected surface. Front and isometric views of the superimposition are shown in figure 4.40. This figure illustrates the parabolic curvature of the reflected surface in its entirety, the presence of the shear layer and the Mach reflection at the wall.

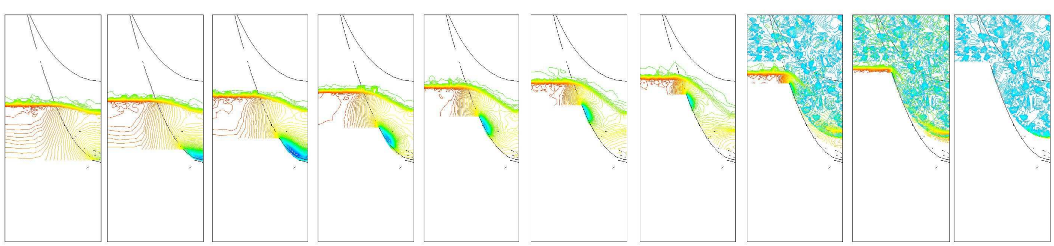

Figure 4.38: Sequential density contour plots for parabolic valley, a = 0.04, taken in the x-y plane in steps of 5mm along the z axis.

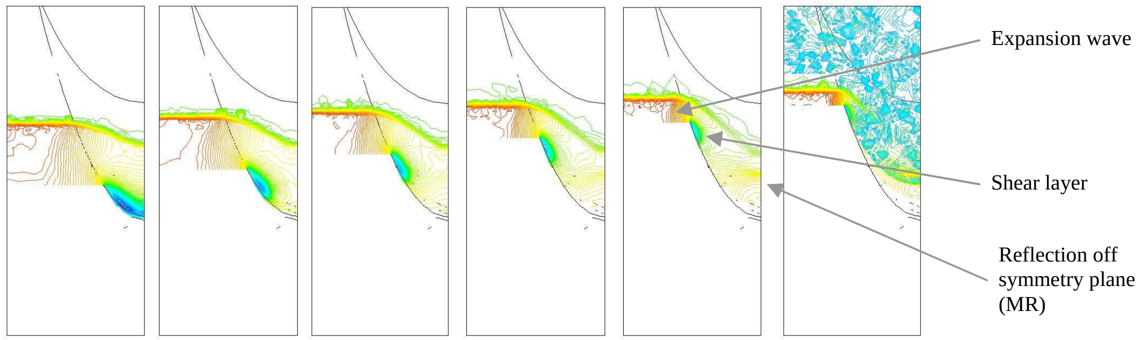

Figure 4.39: Enlarged sequential density contour plots for parabolic valley, a = 0.04, taken in the x-y plane in steps of 5mm along the z axis.

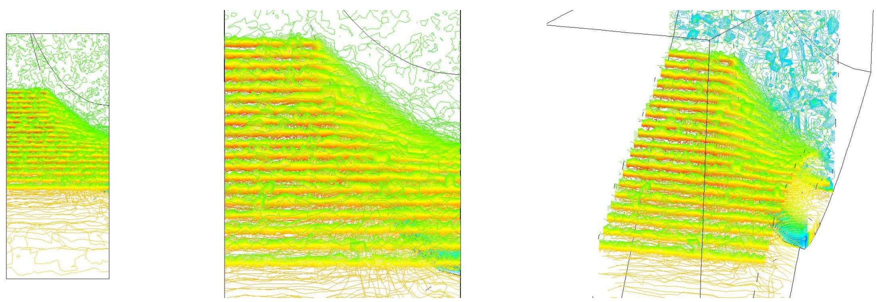

Figure 4.40: Superimposed density contour plots for parabolic valley, a = 0.04, taken in the x-y plane.

To obtain a complete three-dimensional numerical image of the reflected shock surfaces, planes along the x and z axes are superimposed, as shown in figure 4.41. The incident shock, the primary reflected surface, the regular reflection off the wedge, the Mach reflection off the valley floor close to the plane of symmetry and the shear layer at the valley entrance can all be seen in the figure.

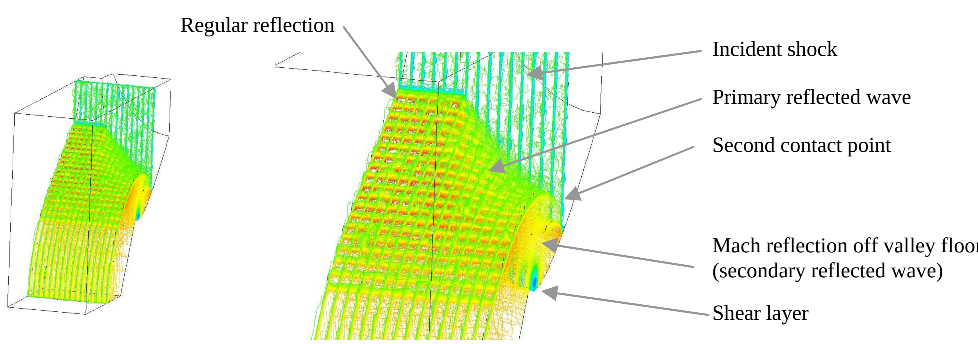

Figure 4.41: Isometric view of superimposed planes for parabolic valley, a = 0.04.

4.5.2 Summary of results for various parabolic valley configurations

Two more parabolic valley configurations were investigated. It was found that the general flow pattern for all parabolic valleys were very similar. The slight differences found in the different configurations due to the various valley characteristic widths are discussed below. The images obtained through experimentation and numerical analysis for these two parabolic valleys is presented in Appendix E3. The different configurations discussed below include where a = 0.055 and a = 0.075 (in the parabolic equation) with a wedge angle of 60 degrees.

Schlieren images taken at sequential time delays showed regular reflection off the wedge as before. The reflected wave from the valley floor reflection is seen upstream of the wedge for all parabolic valley configurations. The suggested three-dimensional wave structure is also depicted from the schlieren images. The sonic wave generated at the valley entrance as well as the effect of the sonic wave from the first corner is seen for all configurations.

Numerical two-dimensional images taken at sequential time steps, similar to figure 4.35, depict regular reflection off the wedge surface and the reflected wave from the valley floor for all parabolic valley configurations. The primary reflected wave is also depicted at the symmetry plane along with the Mach reflection off the valley surface at the plane of symmetry (referred to as the secondary reflected wave) for all parabolic valleys. The shear layer at the valley entrance is depicted for all configurations in these images. The reflected Mach wave off the valley floor forms a semi-circle configuration and makes contact with the valley floor just before the shear layer. The second contact point, found above the triple point, is depicted for all parabolic valley configurations and tends to move down the incident wave as it advances downstream. Once coincident with the triple point, the secondary contact point then moves along the secondary reflected wave surface. The slip stream of the Mach reflection at the symmetry plane is also seen in these images.

Planes along the x axis at a single time step, similar to figure 4.36, are created to determine the geometry of the three-dimensional reflected shock surfaces for all parabolic valleys. The regular reflection off the wedge surface can be seen in the first couple of images. As the incident wave interacts with the valley, regular reflection occurs off the valley floor. As the planes move closer to the symmetry plane, Mach reflection occurs off the valley floor. The Mach stem's characteristic height increases as it nears the symmetry plane. These features are present for all parabolic valley configurations. The second contact point is found as the primary reflected wave flows over in to the valley. The second contact point moves towards the triple point as the planes move closer to the symmetry plane. The Mach reflection found reflecting off the valley floor close to the symmetry plane is seen in the last couple of images. The shear layer is found to cascade down the valley entrance wall for all parabolic configurations.

The three-dimensional secondary reflected wave off the valley floor is similar to that described for the first parabolic valley, figure 4.37. The Mach reflection is found to dissipate, and change to regular reflection as the reflected wave climbs up and along the valley entrance wall for all configurations. The secondary reflected wave surface occurs underneath the primary reflected wave surface found to flow over into the valley. The shear layer cascading down the valley entrance is illustrated well in these images. Once the reflected wave has terminated, the reflection point is found to then travel up along the valley entrance until it meets the regular reflection at the wedge surface.

Front views of planes generated along the z axis, similar to those in figure 4.38, clearly illustrate the shear layer formed at the entrance of the valley for all parabolic valleys. The reflected wave of the Mach reflection off the valley floor is seen, illustrating its reflection geometry in the x-y plane. An expansion wave over the wedge surface is seen for all parabolic valleys. The primary reflected surface is perpendicular to the plane of symmetry, at this plane, for all configurations. By superimposing the planes, a three dimensional image of the primary reflected wave is developed, illustrating the parabolic curvature of the reflected surface which tends to follow the actual geometry of the specific valley.

A complete three-dimensional numerical image of the reflected shock surfaces is developed for each of the parabolic valleys as is shown in figure 4.42. The incident shock, the primary reflected surface, the regular reflection off the wedge, the Mach reflection off the valley floor near the symmetry plane and the shear layer at the valley entrance is seen for all parabolic valley configurations in the figure.

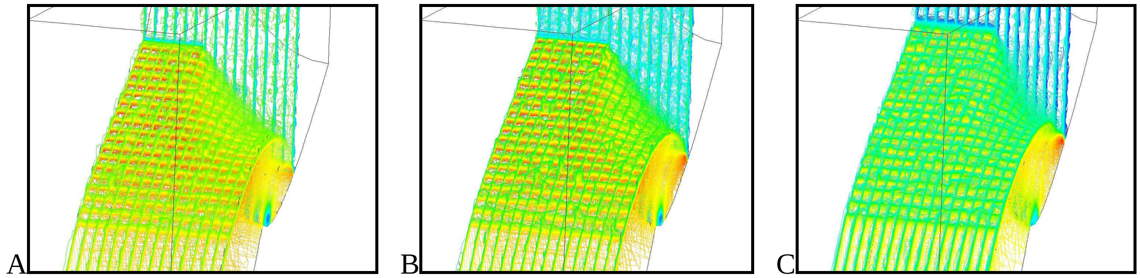

Figure 4.42: Isometric view of superimposed planes for parabolic valleys.

A) a = 0.04 B) a = 0.055 C) a = 0.075

4.6 Conical valley results

4.6.1 Conical valley, 10 degrees

Schlieren images are presented in figure 4.43, taken at sequential time delays. The reflection off the wedge is regular, as expected. The reflection off the valley floor is blocked out in all images for the conical valleys due to the opaque nature of the manufacturing material. However, the reflected wave from the valley floor reflection can be seen upstream of the wedge (very weak). The suggested three-dimensional wave structure can slightly be depicted from the schlieren images. A weak sonic wave generated at the valley entrance can be seen in all schlieren images, as well as the effect of the sonic wave from the first corner. The further downstream the incident shock moves, the greater the influence of the sonic wave becomes on the reflected shock.

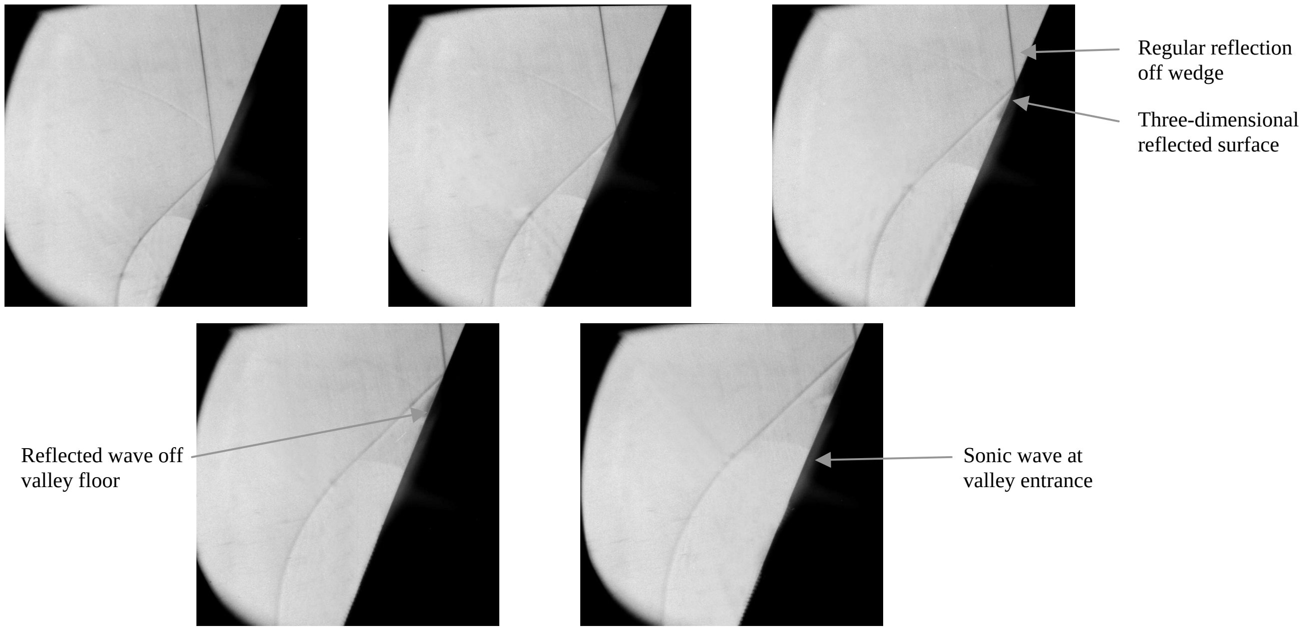

Figure 4.43: Schlieren images for conical valley, 10 degrees, at time delay 1650µs, 1675µs, 1700µs, 1725µs, and 1750µs respectively.

Numerical two-dimensional images were produced from the three-dimensional solution by taking planes at 0mm and 75mm along the x axis. These planes were used in validation of the experimental results for all conical valleys. The two-dimensional images were developed at sequential time steps, allowing direct comparison of the reflection off the wedge and valley surfaces to the schlieren images. The regular reflection off the wedge surface and the reflected wave from the valley floor can be depicted in the images presented in figure 4.44, and compare well with the experimental results. The reflection off the valley surface at the plane of symmetry is Mach reflection. The reflected wave off the valley floor tends to flatten out as the incident shock advances downstream. The effect of the first and second corners on the reflected wave can be seen as the incident shock advances downstream. The presence of a weak shear layer is seen in the last three images, as well as the presence of a weak separation at the valley entrance. The slip stream of the Mach reflection at the symmetry plane can be seen in the last two images.

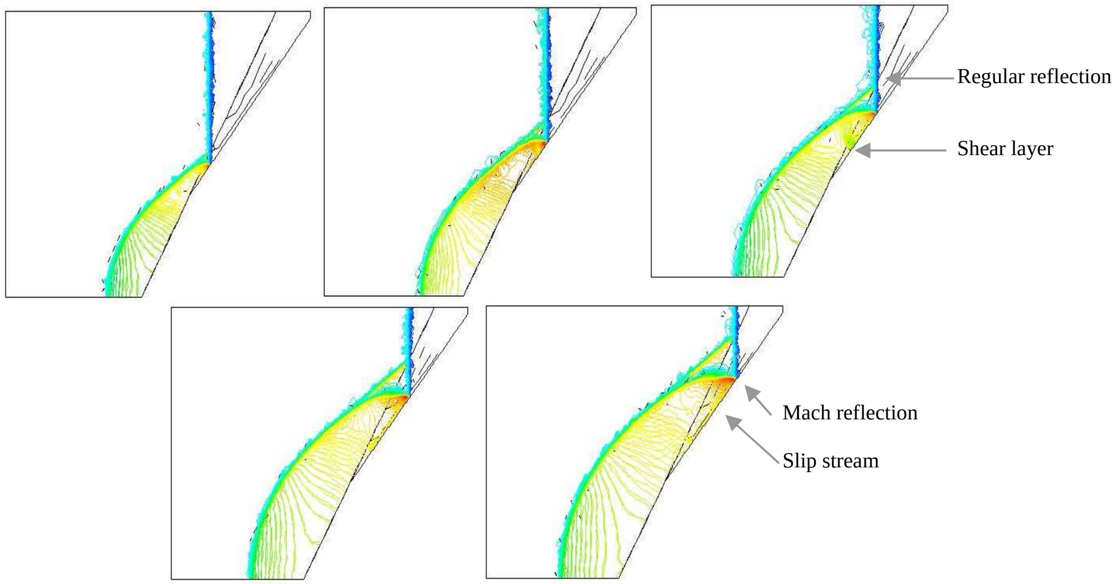

Figure 4.44: Sequential density contour plots for conical valley, 10 degrees.

In order to determine the three-dimensional reflected shock surfaces, planes along the x axis were generated at a single time step. The planes depict how the wave structures change across the width of the test piece. The images can be seen in figure 4.45. The regular reflection off the wedge surface can be seen in the first four images. At the planes close to the valley wall, regular reflection occurs off the valley floor. As the planes move closer to the symmetry plane the regular reflection changes to Mach reflection. The reflected wave from the Mach reflection off the valley floor is referred to as the secondary reflected wave. At the symmetry plane, this secondary reflected wave coincides with the primary reflected wave. The presence of a second contact point on the incident shock is found as the primary reflected wave flows over in to the valley. The second contact point can be seen in the last four images, and moves towards the triple point as the planes move closer to the symmetry plane. The presence of the slip stream and a shear layer cascading down the valley entrance wall are also apparent in the last images.

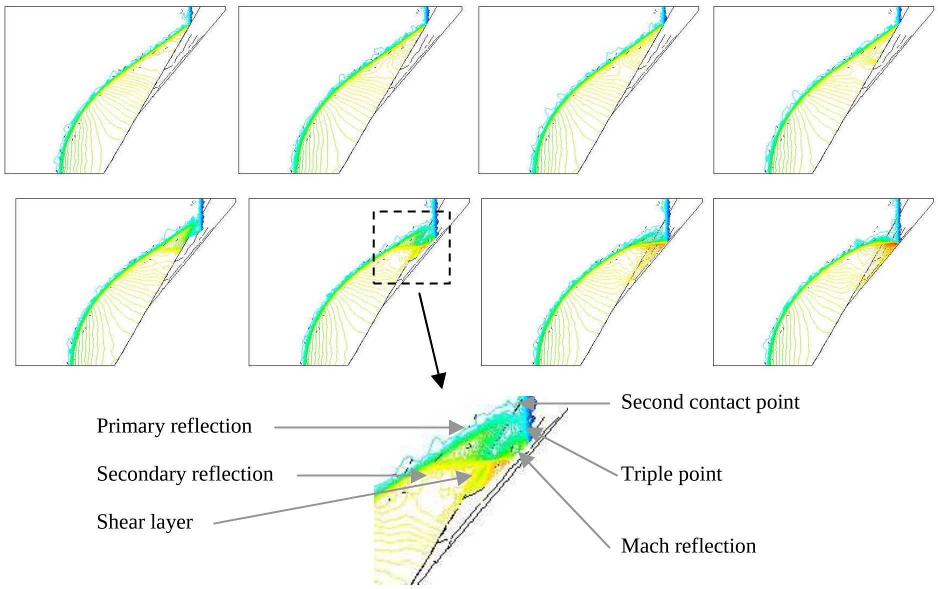

Figure 4.45: Density contour plots for conical valley, 10 degrees, taken in the y-z plane at x = 0mm, 45mm, 50mm, 55mm, 60mm, 65mm, 70mm, 75mm, respectively.

To determine the three-dimensional secondary reflected wave structure off the valley floor, single level pressure contour plots were created. Figure 4.46 was developed by superimposing several planes across the x and z axes. Mach reflection occurs at close proximity to the plane of symmetry. However, as one moves closer to the valley wall the reflection changes to regular. At the same time the reflection point moves along the floor of the valley in curved path. The reflection point then travels up along the valley entrance until it meets the regular reflection at the wedge surface.

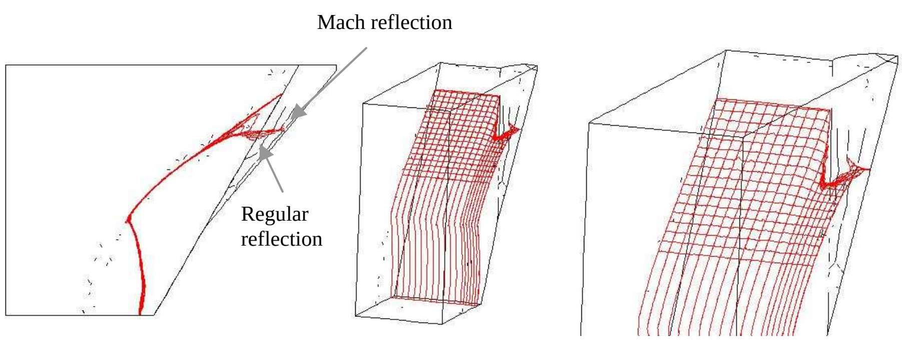

Figure 4.46: Superimposed pressure contour plots (single level) of secondary reflected wave for conical valley, 10 degrees.

To develop a complete three-dimensional understanding of the resulting wave structures, planes along the z axis were generated. Front views of these planes are shown in figure 4.47. Figure 4.48 enlarges the latter images in figure 4.47 to show more detail in the reflection pattern. The sequential planes clearly illustrate the weak shear layer cascading down the valley entrance wall. The planes also illustrate that the curvature of the primary reflected surface tends to become steeper the closer the plane is to the incident shock. A reflection off the plane of symmetry is also depicted in the images. This reflection coincides with the secondary wave surface found in figure 4.45, illustrated in figure 4.46. These images depict this reflection creeping along the wedge surface into the valley and down the valley floor as the planes move further downstream from the valley entrance. An expansion wave over the wedge surface is seen throughout the images. The multiple x-y planes are superimposed to create a three dimensional image of the reflected surface, shown in figure 4.49. This figure illustrates the conical curvature of the primary reflected surface.

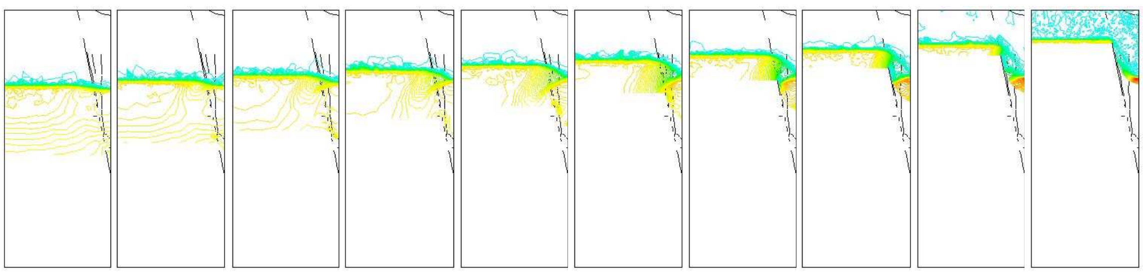

Figure 4.47: Sequential density contour plots for conical valley, 10 degrees, taken in the x-y plane in steps of 5mm along the z axis.

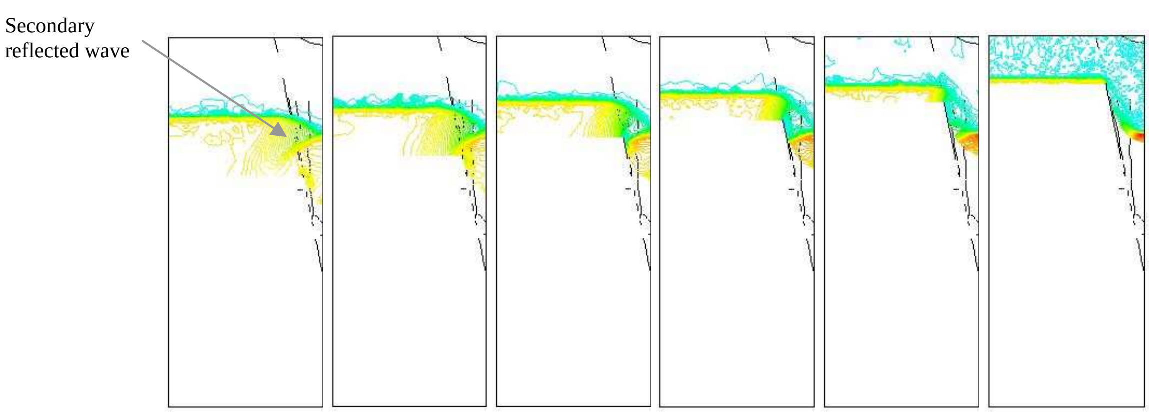

Figure 4.48: Enlarged sequential density contour plots for conical valley, 10 degrees, taken in the x-y plane in steps of 5mm along the z axis.

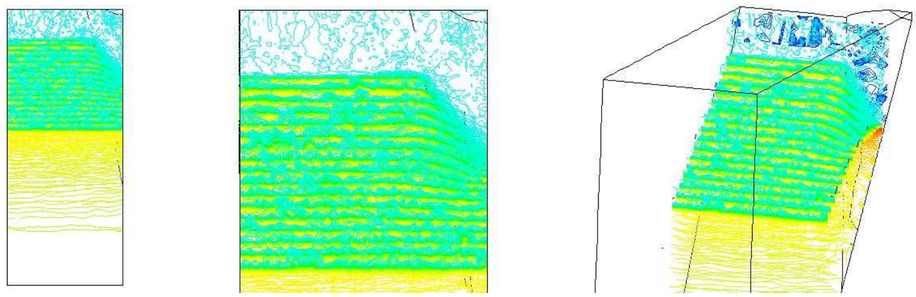

Figure 4.49: Superimposed density contour plots for conical valley, 10 degrees, taken in the x-y plane.

To obtain a complete three-dimensional numerical image of the reflected shock surfaces, planes along the x and z axes are superimposed, as shown in figure 4.50. The incident shock, the primary reflected surface, the regular reflection off the wedge and the Mach reflection off the valley floor near the symmetry plane can all be seen in the figure.

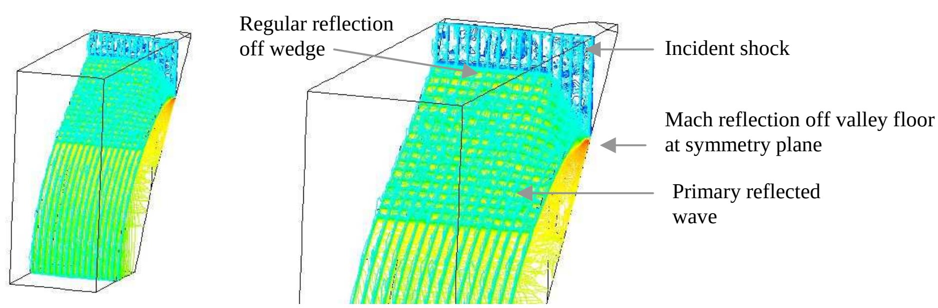

Figure 4.50: Isometric view of superimposed planes for conical valley, 10 degrees.

4.6.2 Summary of results for various conical valley configurations

A second conical configuration of 20 degrees was investigated, with the same wedge angle of 60 degrees. It was found that the general flow pattern for this configuration was very similar to that found for the 10 degree. The images obtained through experimentation and numerical analysis for this conical valley is presented in Appendix E4.

The schlieren images obtained at sequential time delays for the 20 degree conical valley illustrated similar reflection patterns as the 10 degree conical valley. Regular reflection was found to occur off the wedge surface. Once again the reflection off the valley floor could not be depicted but the resulting reflected wave is seen upstream of the wedge. The suggested three-dimensional wave structure is depicted from these images more clearly. The weak sonic wave generated at the valley entrance, as well as the effect of the sonic wave from the first corner is also depicted for this configuration.

The numerical two-dimensional images developed for the 20 degree valley, similar to those found in figure 4.44, compared directly with the experimental images. The images depict regular reflection occurring off the wedge surface and Mach reflection at the plane of symmetry. The reflected Mach wave again tends to straighten out as the incident shock advances downstream. The effect of the first and second corners on the reflected wave is also seen as the incident shock advances downstream. The presence of a weak separation at the valley entrance and the slip stream of the Mach reflection at the plane of symmetry are depicted in the images.

Planes generated along the x axis, similar to those in figure 4.45, showed similar flow patterns to the 10 degree conical valley. Regular reflection occurs off the wedge surface, continuing off the valley floor at planes close to the valley wall. As the planes move closer to the symmetry plane the regular reflection changes to Mach reflection (secondary reflected wave). At the symmetry plane, this secondary reflected wave once again coincides with the primary reflected wave. The presence of a second contact point on the incident shock is found as the primary reflected surface flows over in to the valley. The second contact point again moves towards the triple point as the planes move closer to the symmetry plane. The presence of the slip stream and the shear layer along the valley entrance wall are also apparent in the images.

The three-dimensional secondary wave structure off the valley floor was developed, as in figure 4.46, for the 20 degree conical valley. Again it illustrates Mach reflection occurring close to the plane of symmetry but changing to regular reflection close to the valley wall. At the same time the reflection point moves along the floor of the valley in curved path. The reflection point then travels up along the valley entrance until it meets the regular reflection off the wedge surface.

The front views of planes generated along the z axis were developed, similar to those in figure 4.47. The planes again clearly illustrate the shear layer cascading down the 20 degree conical valley entrance wall. The planes also illustrate that the curvature of the primary reflected surface tends to become steeper the closer the plane is to the incident shock. The reflection off the plane of symmetry is also found for the 20 degree conical valley. This reflection coincides with the secondary wave surface which creeps along the wedge surface into the valley and down the valley floor as the planes move further downstream from the valley entrance. An expansion wave over the wedge surface is again found for this configuration. By superimposing these planes the conical curvature of the primary reflected surface is again illustrated.

A complete three-dimensional numerical image of the reflected shock surfaces for both the conical valley configurations are shown in figure 4.51. The incident shock, the primary reflected surface, the regular reflection off the wedge, the Mach reflection off the valley floor near the symmetry plane, and the conical curvature of the primary reflected wave for both configurations can be seen in the figure. The major differences between the two configurations are the increased Mach stem height, the longer Mach reflection occurrence off the valley floor, the more pronounced shear layer and the primary reflected surface curvature for the 20 degree conical valley.

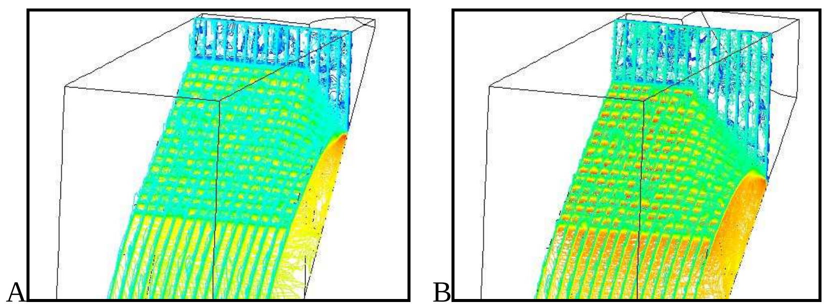

Figure 4.51: Isometric view of superimposed planes for conical valleys.

A) 10 degrees B) 20 degrees

4.7 Hill results

4.7.1 Triangular hill

Schlieren images are presented in figure 4.52, taken at sequential time delays. The reflection off the wedge is regular, as expected. As the incident wave interacts with the triangular hill the resulting regular reflected wave can be seen in the schlieren images. The reflection point off the hill surface can only be seen in the second image otherwise it moves out of range as the incident wave advances. The reflection point of the incident wave on the wedge surface is block out in the images due to the opaque nature of the manufacturing material.

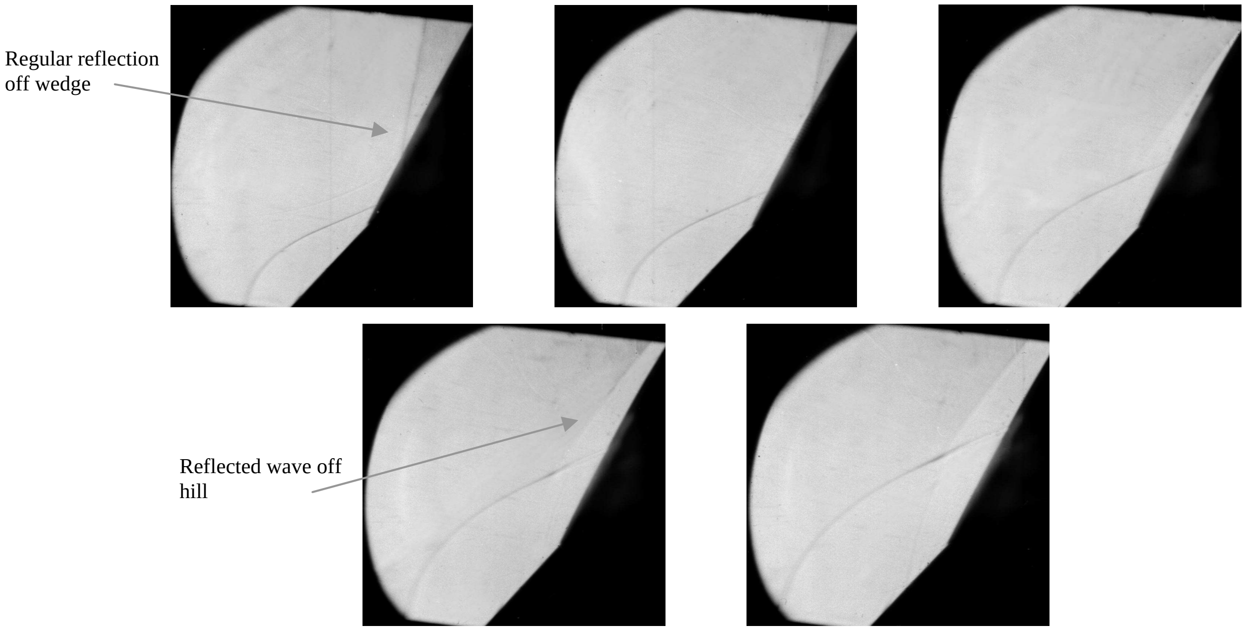

Figure 4.52: Schlieren images for triangular hill, at time delay 1650µs, 1675µs, 1700µs, 1725µs, and 1750µs respectively.

Numerical two-dimensional images were produced with planes at 0mm and 75mm along the x axis. The two-dimensional images were developed at sequential time steps, allowing direct comparison of the reflection off the wedge and hill surfaces to the schlieren images. The reflection off the wedge and hill surfaces can be depicted in the images presented in figure 4.53, and compare directly with the experimental results. The reflection point of the reflection off the hill surface can be seen in the first two images of the figure, there after the point moves out of range. The corner signal generated at the bottom of the wedge is depicted in all the images, increasing in strength as it is compressed over the hill. This compression causes the reflected wave off the wedge to bulge downstream of the reflected wave from the hill.

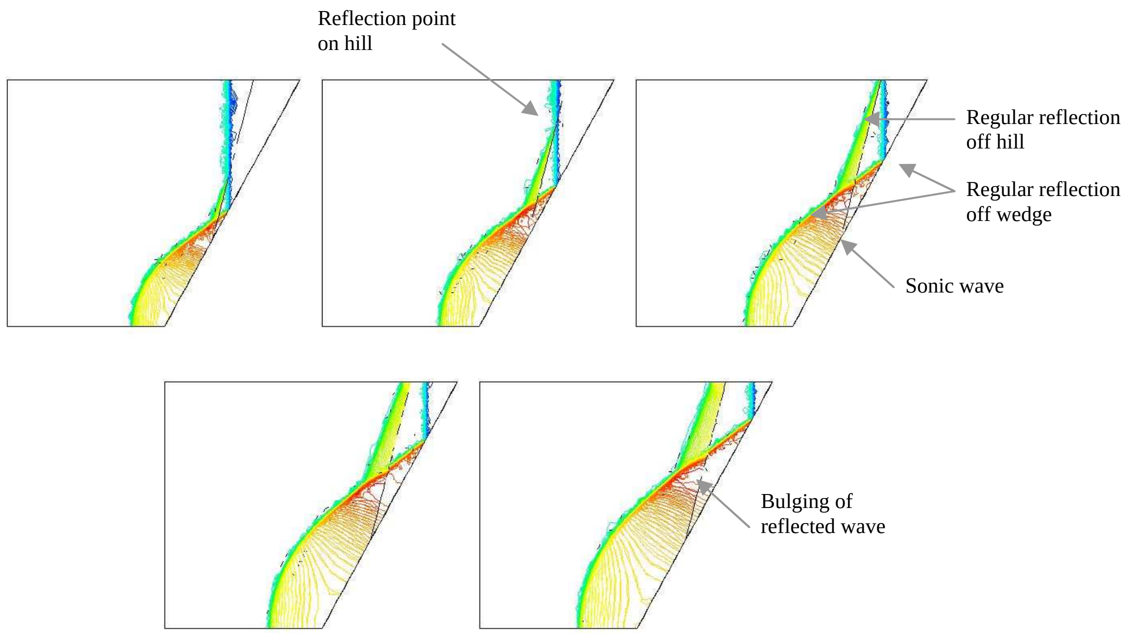

Figure 4.53: Sequential density contour plots for triangular hill.

In order to determine the three-dimensional reflected shock surfaces, planes along the x axis were generated at a single time step. The planes depict how the wave structures change across the width of the test piece. The images can be seen in figure 4.54. The regular reflection off the wedge surface can be seen in the first three images. As the incident wave interacts with the hill, regular reflection occurs off its surface. The reflection point off the hill surface can only be depicted in the fourth and fifth images, it then moves out of range and only the resulting reflected wave can be seen.

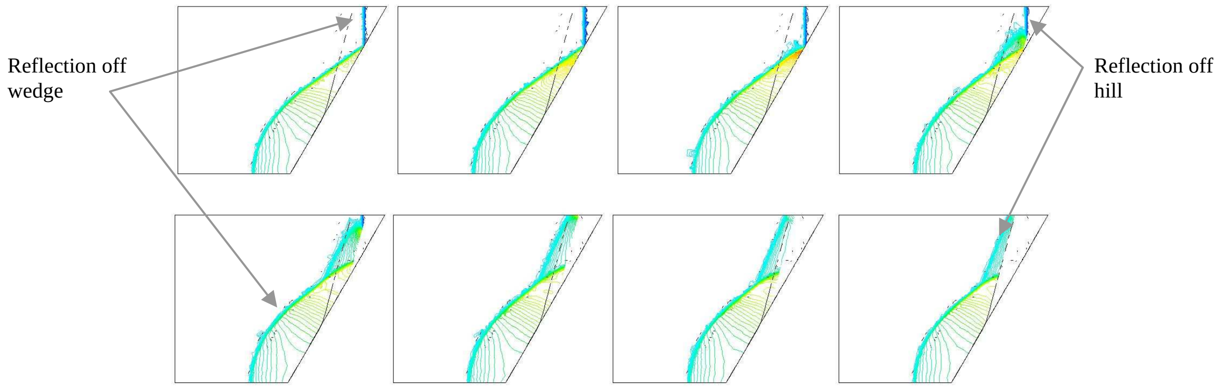

Figure 4.54: Density contour plots for triangular hill, taken in the y-z plane at x = 0mm, 45mm, 50mm, 55mm, 60mm, 65mm,70mm, 75mm, respectively.

To develop a complete three-dimensional understanding of the resulting wave structures, planes along the z axis were generated. Front views of these planes are shown in figure 4.55. The sequential planes illustrate the curved nature of the reflected wave from the hill surface. The planes clearly illustrate a Mach stem forming where the reflected surfaces from the wedge and hill amalgamate. Therefore, the reflected waves essentially become the incident waves of the Mach reflections. Two triple points result, with a Mach stem developing on the wedge surface and another Mach stem developing on the hill surface. The Mach stem surfaces, in a three-dimensional sense form a lopsided upside down U shape surface, initially starting off with a wide entrance upstream and closing up to a point at the incident wave.

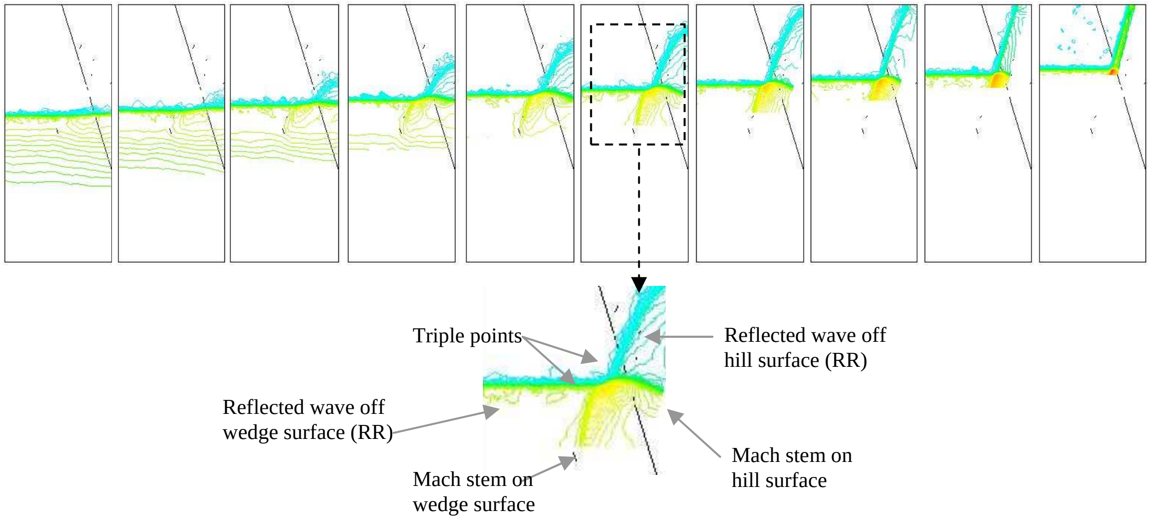

Figure 4.55: Sequential density contour plots for triangular hill, taken in the x-y plane in steps of 5mm along the z axis.

To obtain a complete three-dimensional numerical image of the reflected shock surfaces, planes along the x and z axes are superimposed, as shown in figure 4.56. The incident shock, the wedge reflected surface, the hill reflected surface and the Mach stem off the hill can all be seen in the figure.

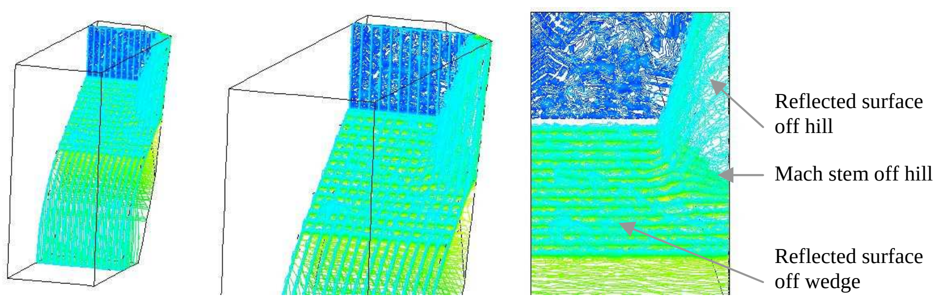

Figure 4.56: Isometric view of superimposed planes for triangular hill.

4.7.2 Summary of results for various hill configurations

Two more hill configurations were investigated, parabolic and conical, with the same wedge angle of 60 degrees. It was found that the general flow patterns for these configurations were very similar to that found for the triangular hill. The images obtained through experimentation and numerical analysis for these two hill configurations are presented in Appendix E5.

Schlieren images obtained for the parabolic and conical hills are similar to those found in figure 4.52. The regular reflection off the wedge surface is seen for the first time delays. As the incident wave advances downstream regular reflection occurs off the hill surface as well. The reflection point for both the parabolic and conical wedge surfaces is visible in the first images becoming blocked out by the opaque nature of the manufacturing material as the incident wave advances. The reflection point off the hill surfaces is seen clearly for these configurations until they move out of range. The resulting reflected wave follows a similar contour as the hill. As the incident wave advances downstream, a resulting double triple point is seen for both configurations. The triple points tend to migrate away from each other as the incident wave advances. The Mach stems generated from the triple points, one contacting the wedge surface and one the hill surface, are also seen in the images. In the last images the generation of a corner signal at the top of the wedge is seen.

Numerical two-dimensional images at sequential time delays were produced for the parabolic and conical hills, similar to those in figure 4.53. The two-dimensional images compared directly to the experimental findings. The regular reflection off the wedge and hill surfaces is depicted in the images. The reflection point of the reflection off the hill surface can be seen in the first images, there after the point moves out of range. The corner signal generated at the bottom of the wedge is depicted in all the images. The generation of the double triple point and the resulting Mach stems is seen clearly for the parabolic hill. The Mach stems are curved, one initiating from the wedge surface the other from the hill surface. A corner signal is seen for both configurations at the top of the wedge. A weak influence of a corner signal generated at the base of the conical hill is seen in the images.

In order to determine the three-dimensional reflected shock surfaces, planes along the x axis were generated at a single time step for both configurations, similar to those presented in figure 5.54. The regular reflection off the wedge surface is seen in the first few images for both configurations. As the incident wave interacts with the hill, regular reflection occurs off its surface. The reflection point off the hill surface could only be depicted in one of the images for the conical hill, otherwise it moved out of range and only the resulting reflected wave is seen. The double triple point for the parabolic hill can again be seen in the images as the incident wave interacts with the hill. The resulting Mach stem are also depicted in the images, as well as the corner signal generated at the top of the hill. This corner signal is also present for the conical hill.

To develop a complete three-dimensional understanding of the resulting wave structures for both the parabolic and conical hills, front view images similar to figure 5.55 were developed. The sequential planes illustrate the curved nature of the reflected wave from the hill surface. The planes clearly illustrate the double triple point and the two Mach stems found for both the parabolic and conical hills. The double triple point is seen to form where the reflected surfaces from the wedge and hill amalgamate, resulting in one Mach stem developing on the wedge surface and the other developing on the hill surface, as before. The Mach stem surfaces, in a three-dimensional sense form a V (on its side) shaped surface with one side of the V rounded for the parabolic hill and a lopsided upside down U shaped surface for the conical hill. The surfaces both initially start off with a wide entrance upstream, closing up to a point at the incident wave. This surface is much narrower for the conical hill.

To obtain a complete three-dimensional numerical image of the reflected shock surfaces for all the hill configurations, planes along the x and z axes are superimposed, as shown in figure 4.57. The incident shock, the wedge reflected surface, the hill reflected surface and the Mach stem off the hill are all seen in the figure.

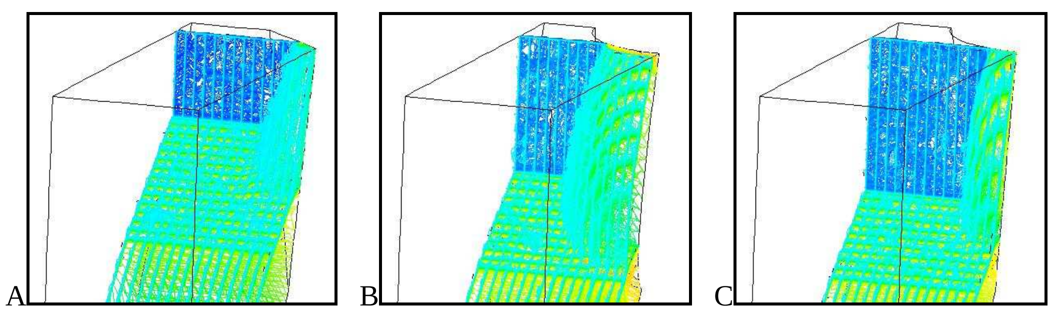

Figure 4.57: Isometric view of superimposed planes for hill configurations.

A) Triangular hill B) Parabolic hill C) Conical hill